

Enzyme-inhibitor-like tuning of Ca²⁺ channel connectivity with calmodulin

Xiaodong Liu¹, Philemon S. Yang¹, Wanjun Yang¹ & David T. Yue¹

Ca²⁺ channels and calmodulin (CaM) are two prominent signalling hubs¹ that synergistically affect functions as diverse as cardiac excitability², synaptic plasticity³ and gene transcription⁴. It is therefore fitting that these hubs are in some sense coordinated, as the opening of Ca_v1–2 Ca²⁺ channels are regulated by a single CaM constitutively complexed with channels⁵. The Ca²⁺-free form of CaM (apoCaM) is already pre-associated with the isoleucine–glutamine (IQ) domain on the channel carboxy terminus, and subsequent Ca²⁺ binding to this ‘resident’ CaM drives conformational changes that then trigger regulation of channel opening⁶. Another potential avenue for channel–CaM coordination could arise from the absence of Ca²⁺ regulation in channels lacking a pre-associated CaM^{6,7}. Natural fluctuations in CaM concentrations might then influence the fraction of regulable channels and, thereby, the overall strength of Ca²⁺ feedback. However, the prevailing view has been that the ultrastrong affinity of channels for apoCaM ensures their saturation with CaM⁸, yielding a significant form of concentration independence between Ca²⁺ channels and CaM. Here we show that significant exceptions to this autonomy exist, by combining electrophysiology (to characterize channel regulation) with optical fluorescence resonance energy transfer (FRET) sensor determination of free-apoCaM concentration in live cells⁹. This approach translates quantitative CaM biochemistry from the traditional test-tube context into the realm of functioning holochannels within intact cells. From this perspective, we find that long splice forms of Ca_v1.3 and Ca_v1.4 channels include a distal carboxy tail^{10–12} that resembles an enzyme competitive inhibitor that retunes channel affinity for apoCaM such that natural CaM variations affect the strength of Ca²⁺ feedback modulation. Given the ubiquity of these channels^{13,14}, the connection between ambient CaM levels and Ca²⁺ entry through channels is broadly significant for Ca²⁺ homeostasis. Strategies such as ours promise key advances for the *in situ* analysis of signalling molecules resistant to *in vitro* reconstitution, such as Ca²⁺ channels.

Our investigations build on a Ca_v1.4 channel mutation underlying congenital stationary night blindness¹⁵. This mutation yields a premature stop that deletes the distal carboxy tail (DCT) of these retinal Ca²⁺ channels, and produces an unexpected emergence of their Ca²⁺ regulation by CaM^{11,12}, known as Ca²⁺-dependent inactivation (CDI). Full-length Ca_v1.4 channels lack CDI^{11,12}, thereby maintaining Ca²⁺-driven transmitter release at tonically depolarized retinal synapses. Hence, the emergence of CDI probably impairs vision. Mechanistically, the DCT contains a CDI-inhibiting module (ICDI) that is reported to somehow ‘switch off’ the latent CDI of Ca_v1.4 channels^{11,12}.

Figure 1 summarizes our initial characterization of ICDI effects. Because Ca_v1.4 channels yield diminutive currents¹⁶, we appended the DCT of the main Ca_v1.4 subunit (α_{1F}) onto the core of better-expressing Ca_v1.3 channels (main subunit, α_{1D}). This approach

permits robust investigation of DCT effects^{11,12}. As baseline, Fig. 1a displays the CDI of core Ca_v1.3 channels (left, $\alpha_{1D\Delta}$), similar to natural short splice variants⁸. Core channels contain all elements required for CDI^{6,17}, including the IQ domain for apoCaM pre-association⁶ and the EF-hand-like region for CDI transduction¹⁸. Depolarization thereby produced a rapidly decaying Ca²⁺ current (middle, red trace), indicative of strong CDI. Because Ba²⁺ binds CaM poorly¹⁷, the slow Ba²⁺ current decay (middle, black trace) represents the background inactivation of a distinct voltage-dependent process^{6,7}. Thus, the fraction of peak current remaining after depolarization for 50 ms (right, r_{50}) relates intimately to inactivation, with the difference between the Ca²⁺ and Ba²⁺ r_{50} relations indexing CDI (f_{50}). Appending the Ca_v1.4 DCT to the Ca_v1.3 core (Fig. 1b, left) significantly reduced CDI (middle and right) relative to control (dashes) (Supplementary Information, section 1.2). Notably, the DCT did not altogether abolish CDI as reported before^{11,12}, but left a clear residuum. This difference foreshadowed major mechanistic and biological consequences.

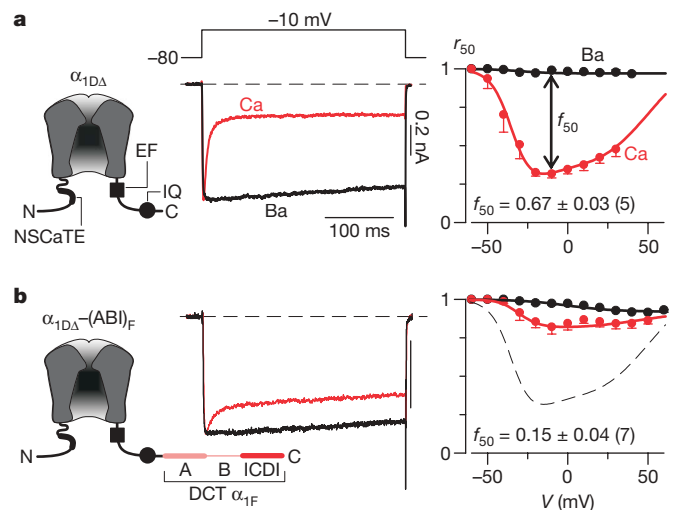


Figure 1 | Distal carboxy tail of Ca_v1.4 weakens Ca²⁺ regulation of channels. **a**, Core Ca_v1.3 channel contains all known structural elements required for CDI (schematic of main subunit $\alpha_{1D\Delta}$, containing NSCaTE¹⁷, EF¹⁸ and IQ⁶) and thereby exhibits robust CDI (subpanels). Average f_{50} CDI metric shown at bottom (data shown, mean \pm s.e.m.), with number of cells in parentheses. Throughout, current scale bars pertain to Ca²⁺ currents. Ba²⁺ currents are scaled for kinetic comparison. Tail currents are clipped to frame. **b**, Adding DCT of α_{1F} (main pore-forming Ca_v1.4 subunit) to core Ca_v1.3 channel weakens CDI. A, B and ICDI segments of the α_{1F} DCT (together referred to as (ABI)_F) are defined in Supplementary Information, section 1.1. The dashed curve reproduces the baseline from **a**.

¹Calcium Signals Laboratory, Departments of Biomedical Engineering and Neuroscience, The Johns Hopkins University School of Medicine, Ross Building, Room 713, 720 Rutland Avenue, Baltimore, Maryland 21205, USA.

Hints of these consequences came from qualitative consideration of underlying mechanism. As background, we recapitulated coarse structural underpinnings of DCT effects. To confirm that DCT function requires complementary elements within core channels^{11,12}, we showed the lack of DCT effects on Ca_v2.2 channels (Supplementary Information, section 1.3), which presumably lack complementing modules. Furthermore^{10,12}, when such complementing modules are present, only ICDI and A subsegments of the DCT (Fig. 1b, left) are required for inhibition of CDI (Supplementary Information, section 1.4). Beyond these initial points, actual DCT mechanisms remain controversial. Glutathione S-transferase pull-downs of channel peptides have been used to support an allosteric mechanism (Supplementary Information, section 1.5), in which the ICDI associates with an EF-hand-like module to eliminate CDI transduction¹² (Fig. 1a, left), but leaves apoCaM–channel binding unchanged. By contrast, in other work, channel peptide FRET has been used to advance a competitive mechanism (Supplementary Information, section 1.5) in which ICDI competes with apoCaM for binding near the channel IQ domain (Fig. 1a, left), thus inhibiting CDI by displacing CaM from channels¹¹.

To help resolve this controversy, we pursued two preliminary approaches. First, using live-cell FRET two-hybrid assays^{6,17} we tested whether the Ca_v1.4 ICDI (Fig. 2a, cyan fluorescent protein (CFP) fused to ICDI (ECFP–ICDI_F), could bind the presumed apoCaM pre-association module of Ca_v1.3 (yellow fluorescent protein (YFP) fused to the PreIQ₃–IQ–A segment of the channel, as schematized in Figs 1b and 2a (EYFP–PreIQ₃–IQ_D–A_F); Supplementary Information, section 2.1). We thus resolved a high-affinity *in situ* binding curve (Fig. 2a) in which FRET strength (FR) is plotted cell-by-cell versus the concentration of free ECFP–ICDI_F (D_{free} , free donor). By contrast to previous analyses using single-number FRET indices¹¹, our binding curve excludes low-affinity interaction, and a similar binding curve was obtained for partners solely derived from Ca_v1.4 (Supplementary Information, section 2.2). We also confirmed avid binding between apoCaM (ECFP–CaM_{WT} in resting cells) and this EYFP–PreIQ₃–IQ_D–A_F module⁶ (Fig. 2b). More telling, the ICDI (without a fluorophore) attenuated the same apoCaM interaction (Fig. 2c, grey zone), suggesting that ICDI and apoCaM could vie for IQ occupancy (Supplementary Fig. 2.2b). Together, these data confirmed the potential for competition but pertained only to peptides, without guarantee of analogous events within intact channels.

Accordingly, a second provisional approach specifically targeted the holochannel configuration. Scrutiny of mechanisms (Supplementary Information, section 1.5) showed that manipulating apoCaM concentrations would affect CDI only in the competitive, but not strictly allosteric, framework. Indeed, increasing the CaM concentration sharply reversed ICDI effects (Fig. 2d, middle), and apoCaM chelation eliminated residual CDI (Fig. 2d, right; Supplementary Information, section 2.3). Notably, increasing the CaM concentration also increased the CDI of full-length Ca_v1.4 channels (Fig. 2e; but see ref. 19). Overall, both preliminary approaches supported competition, and the residual CDI seen earlier (Fig. 1b) appeared to reflect incomplete competition. Still, these data neither excluded more nuanced allosteric mechanisms²⁰ nor revealed whether biologically relevant CaM fluctuations could modulate CDI.

These limitations might be overcome if only the free-apoCaM concentration could be quantified within the same cells where CDI was measured. Then the holochannel equivalent of classic enzyme inhibition plots²⁰, which rigorously distinguish among mechanisms, could be determined. Accordingly, we incorporated a recently developed optical FRET-based sensor of apoCaM, BSCaM_{IQ}. Here CFP and YFP flank the apoCaM-binding site of neuromodulin⁹ (Fig. 3a), such that the overall FRET is determined by the free-apoCaM concentration. We confirmed the limiting behaviours by co-expressing BSCaM_{IQ} with excess CaM (Fig. 3b, blue line) or CaM-chelating peptides (Fig. 3b, green line (FR_{max}); Supplementary Information, section 3.1). As expected, FR was nearly independent

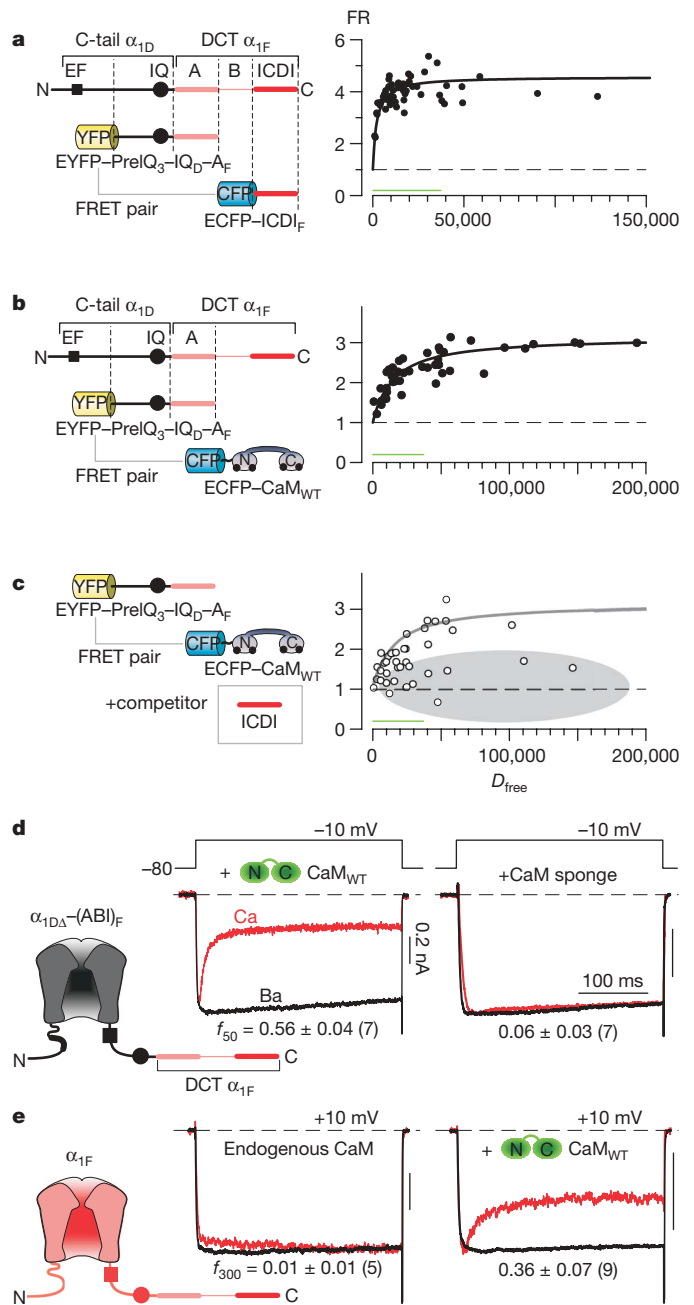


Figure 2 | Provisional evidence for competition. **a**, FRET, CFP-tagged ICDI of α_{1F} versus YFP-tagged PreIQ₃–IQ–A from Fig. 1b (Supplementary Information, section 2.1). FR is proportional to the product of FRET efficiency and fraction of YFP-tagged molecules bound⁶. D_{free} relative concentration of unbound CFP-tagged molecules; scale bar (green), ~500 nM (ref. 6). **b**, FRET, apoCaM versus PreIQ₃–IQ–A in **a**. **c**, ICDI (without fluorophore) attenuates binding in **b**. The grey reference curve is from **b**. **d**, Left, CDI is rescued upon overexpressing CaM with chimera in Fig. 1b. Right, CaM sponge (Ca_v1.2 YFP–PreIQ₃–IQ⁶) eliminates CDI. **e**, Overexpressing CaM with full-length Ca_v1.4. f_{300} , 300-ms version of f_{50} .

of isolated CFP fluorescence, which is an approximate measure of sensor expression in each cell. By contrast, when BSCaM_{IQ} was expressed alone, FR increased towards FR_{max} (Fig. 3b, black line), as anticipated for a sensor that chelates and decreases free apoCaM. With reassurance of BSCaM_{IQ} performance in our system, we co-expressed BSCaM_{IQ} and Ca²⁺ channels, and measured the free-apoCaM concentration before determining CDI in the same cell (Fig. 3c). If free apoCaM were varied among cells by CaM overexpression or chelation, the resulting plot of CDI versus apoCaM would rigorously distinguish among mechanisms. Specifically, using the

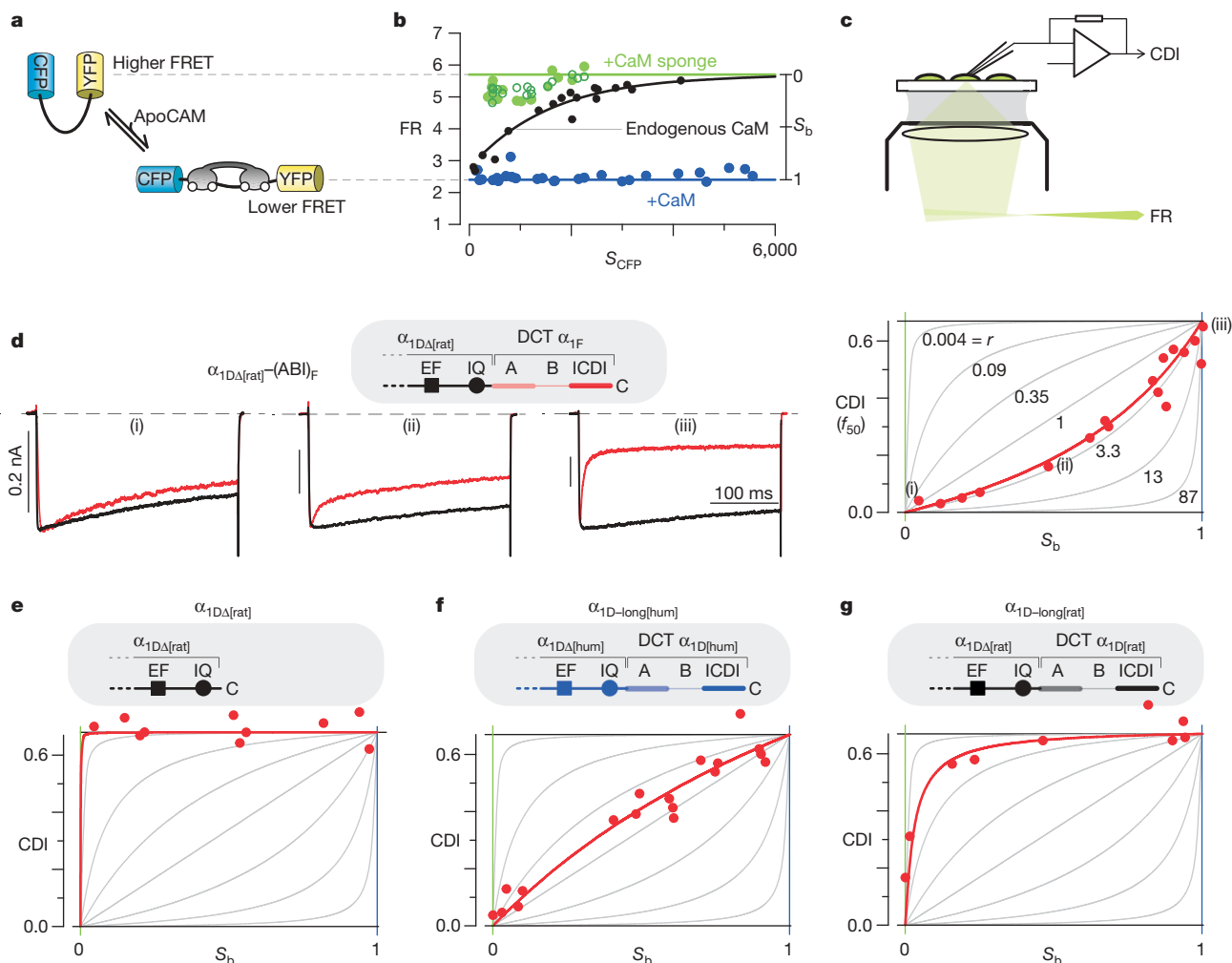


Figure 3 | Live-cell holochannel biochemistry proves competition.

a, BSCaM_{1Q} schematic. **b**, BSCaM_{1Q} expressed alone (black curve and data points) and co-expressed with CaM or CaM sponges (neuromodulin IQ (filled green data points; Supplementary Information, section 3.1) or Cav1.2 PreIQ₃-IQ⁶ (open green data points)). S_{CFP} , isolated CFP fluorescence⁶. **c**, Approach to obtaining CDI and FRET read-outs of apoCaM (FR) in single

relation between FRET and free-apoCaM concentration in our cells⁹ (Supplementary Information, section 3.2), the exact signature of competition²⁰ becomes as shown in the right-hand plot of Fig. 3d (grey curves) and

$$\text{CDI} = \text{CDI}_{\text{max}} \frac{S_b}{S_b(1-r) + r} \quad (1)$$

where $r = K_{\text{d-channel-apparent}}/K_{\text{d-sensor}}$. CDI_{max} is the maximal CDI without ICDI, $K_{\text{d-channel-apparent}}$ is the apparent dissociation constant of channels for apoCaM (with competitive inhibitor), $K_{\text{d-sensor}}$ is the dissociation constant of BSCaM_{1Q} for apoCaM⁹ (2.3 μM), and S_b is the fraction of sensor bound to apoCaM (Supplementary Information, section 3.3). As Fig. 3b shows, S_b is directly determined from FR and ranges from zero to one with increasing apoCaM. If ICDI competition is strong ($r > 1$), curves will be upwardly concave (right-hand plot of Fig. 3d, grey curves); if it is weak ($r < 1$), curves will be downwardly concave.

Figure 3d also displays the experimental outcome for core Cav1.3 channels affixed to the Cav1.4 DCT ($\alpha_{1\text{D}\Delta}$ -(ABI)_F, from Fig. 1b). In the CDI- S_b plot, each symbol corresponds to a single cell, and together these data fit the competitive scheme (red curve; equation (1)) remarkably well. Current traces from exemplar cells (left-hand plots of Fig. 3d; (i)–(iii)) explicitly demonstrate the appropriate increase of CDI with increasing S_b and apoCaM concentration. Importantly,

cells. **d**, CDI- S_b analysis for $\alpha_{1\text{D}\Delta}$ -(ABI)_F, for -10-mV steps. Right, grey CDI- S_b curves illustrate potential profiles for competitive inhibition, according to equation (1). The superimposed red data points and fit conform to the competitive profile. Left, corresponding exemplar traces, labelled (i)–(iii). **e–g**, CDI- S_b analysis for $\alpha_{1\text{D}\Delta}$ -(ABI)_F, $\alpha_{1\text{D-long}}$ -(ABI)_F and $\alpha_{1\text{D-long}}$ -(ABI)_F (the rat orthologue of $\alpha_{1\text{D-long}}$ -(ABI)_F); format as in **d**.

parallel analysis of core Cav1.3 channels revealed far greater apoCaM affinity (Fig. 3e), yielding maximal CDI throughout. Hence, the upward concavity in Fig. 3d is a genuine ICDI effect, not an unanticipated property of the Cav1.3 core. Critically, at high apoCaM concentration ($S_b \approx 1$), the CDIs of the two constructs converged, which is a hallmark of competition²⁰.

Having established these results for the retinal Cav1.4 DCT, we wondered whether CDI- S_b analysis might uncover similar DCT mechanisms in other Ca²⁺ channel subtypes, with yet broader distribution and impact. We considered a long splice variant of the human Cav1.3 channel¹⁰ ($\alpha_{1\text{D-long}}$ -(ABI)_F), which contains a DCT homologous to that in Cav1.4. This long variant has recently been reported to have decreased CDI¹⁰ in comparison with a short variant akin to core channels (see, for example, Fig. 3e). It thus seemed plausible that a competitive ICDI mechanism could extend to these channels, which would be an important possibility given the wide distribution of Cav1.3 channels^{13,14} and the predominance of the long variant throughout brain¹⁰. Complicating this view, however, were our prior observations that corresponding long and short variants of rat Cav1.3 channels show no difference in CDI⁸. Indeed, all of the experiments described to this point of the present study involved constructs based on rat Cav1.3 channels. Accordingly, we undertook CDI- S_b analysis of long Cav1.3 variants from both human and rat. The human long Cav1.3 variant (Fig. 3f) adhered to a competitive ICDI mechanism,

with maximal CDI equivalent to that of core channels (compare Fig. 3f with Fig. 3e). This suggests that long forms of $\text{Ca}_v1.3$ and $\text{Ca}_v1.4$ channels do share a common ICDI mechanism. However, the CDI- S_b relation for the human long $\text{Ca}_v1.3$ variant differs quantitatively from that with the $\text{Ca}_v1.4$ DCT (compare Fig. 3f with Fig. 3d), indicating that the strength of ICDI competition is customized according to channel isoform. Indeed, the rat long $\text{Ca}_v1.3$ variant showed extreme customization (Fig. 3g). Here CDI- S_b analysis unmasks competitive inhibition, but the competition is weak enough that CDI remains maximal, except with overt chelation of apoCaM (at $S_b \approx 0$). The steep saturation of this CDI- S_b relation thus explains prior data showing that CDI was unaffected by the rat $\text{Ca}_v1.3$ DCT, as no depletion was used⁸. Importantly, the CDI- S_b curve for the rat long variant (Fig. 3g) is distinct from that for the $\text{Ca}_v1.3$ core (Fig. 3e), where CDI stayed maximal throughout. Hence, the presence of rat $\text{Ca}_v1.3$ DCT entails customization, not elimination of the competitive inhibitory mechanism (Supplementary Information, section 3.4).

The similarity of DCT elements, particularly of human and rat $\text{Ca}_v1.3$, suggested that minute differences produce extremes of tuning. Indeed, we found that a single valine-to-alanine switch within the ICDI explains the difference (human:rat, ICDI position 47; Supplementary Information, section 3.5).

Although the CDI- S_b analysis established a competitive inhibitory mechanism at the holochannel level, still critically unresolved was whether the ICDI/IQ peptide interactions studied so far (Fig. 2c)

were relevant to holochannel competition, especially given the multiplicity of CaM sites in channels^{6,17,21,22}. This is a generic challenge for large signalling complexes. Importantly, enzyme analysis could be extended to resolve even this ambiguity. Figure 4a summarizes our data for competitive inhibition in holochannels, recasting CDI- S_b data into classic reciprocal-plot form²⁰, where channel CDI (f_{50}) corresponds to enzyme catalytic velocity, V , and apoCaM corresponds to enzyme substrate concentration, S . Visual accord with the textbook signature of competition underscores the insights already provided by *in situ* holochannel biochemistry. Beyond this, if ICDI/IQ binding actually underlies holochannel competition, enzyme analysis additionally predicts a linear relation between the apparent apoCaM dissociation constant for holochannels ($K_{d\text{-channel-apparent}}$; equation (1)) and the reciprocal of the peptide dissociation constant ($1/K_{d\text{-FRET-peptide}}$):

$$K_{d\text{-channel-apparent}} = \frac{K_{d\text{-channel}}[\text{ICDI}]}{K_{d\text{-FRET-peptide}}} + K_{d\text{-channel}}$$

Here $K_{d\text{-channel}}$ is the holochannel dissociation constant for apoCaM without inhibitor and [ICDI] is the effective concentration of ICDI at the channel pre-association site for apoCaM²⁰ (Supplementary Information, section 4.1). Conversely, if peptide interactions are peripheral or the inhibitory mechanism not strictly competitive, this relation will probably fail (Supplementary Information, section 4.2). To test this prediction, we noted that CDI- S_b analysis had already determined

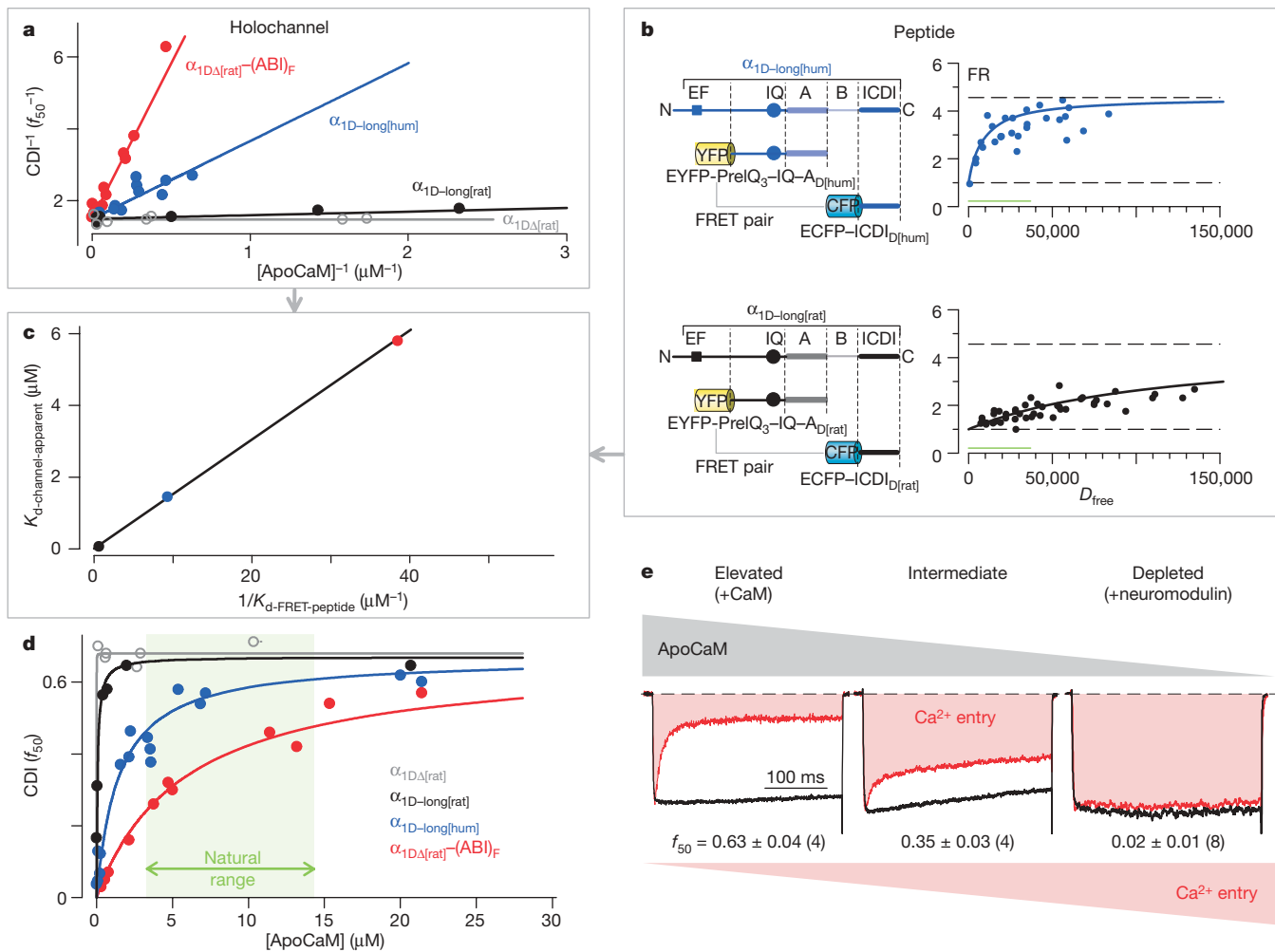


Figure 4 | Molecular interactions and biology of competitive inhibitory tuning. **a**, Reciprocal-plot representation of the relations in Fig. 3d–g. **b**, FRET assays characterizing presumed peptide interactions underlying holochannel competition (as in **a**). **c**, Linear relation between holochannel and peptide competition parameters. **d**, Linear format of quantitative tuning

relations. Natural range (green), 99% boundaries²³. **e**, Consequences of connectivity in the long variant of human $\text{Ca}_v1.3$. Natural variability of native CaM buffers (neuromodulin) affects CDI and Ca^{2+} entry for the long variant of human $\text{Ca}_v1.3$. Left, CaM co-expression; middle, endogenous CaM; right, neuromodulin co-expression.

$K_{d\text{-channel-apparent}}$ for channels with three different ICDIs (Figs 3d, f, g and Fig. 4a). Also, $K_{d\text{-FRET-peptide}}$ for the $\text{Ca}_v1.4$ ICDI was measured in Fig. 2a and the remaining $K_{d\text{-FRET-peptide}}$ values are deduced in Fig. 4b. The resulting linear plot (Fig. 4c) indicates that ICDI/IQ binding does underlie holochannel competition, and that apoCaM pre-association with channels involves the IQ domain with $K_{d\text{-channel}} \approx 10$ nM (Fig. 3e and Supplementary Information, section 4.1).

Transforming the reciprocal plots (Fig. 4a) into normal format raises diverse biological issues (Fig. 4d). The dogma has been that Ca^{2+} channels have an ultrastrong apoCaM affinity⁸, ensuring maximal CDI over the natural range²³ (green), as confirmed for channels lacking ICDI (Fig. 4d, grey curve). Earlier reports that ICDI simply 'switches off' CDI^{11,12} further promoted this perceived dissociation of CDI and apoCaM fluctuations. By contrast, we show here that ICDI returns CDI-[apoCaM] relations, such that natural variations of apoCaM modulate CDI and overall Ca^{2+} entry (Fig. 4d). Such interconnection opens many new possibilities, given the widespread impact and distribution of $\text{Ca}_v1.3$ and $\text{Ca}_v1.4$ channels^{13–15}, and the regulation of CaM²³. For example, co-expressing neuromodulin (a biomolecule that affects synaptic growth/remodelling/plasticity and buffers apoCaM²⁴) with the long variant of human $\text{Ca}_v1.3$ channels decreases apoCaM concentration sufficiently to eliminate CDI and promote Ca^{2+} entry (Fig. 4e and Supplementary Information, section 4.3). This outcome may bear on schizophrenia, in which the concentration of hippocampal neuromodulin is decreased²⁵. Moreover, neurodegenerative diseases are potentially associated with Ca^{2+} dysregulation and, thereby, altered apoCaM²⁶. In Parkinson's disease, excess α -synuclein is pathogenic²⁷, these molecules bind apoCaM²⁸, and elevated substantia nigral $\text{Ca}_v1.3$ activity predisposes for disease²⁹. In Alzheimer's disease, CaM is depleted²⁶. More broadly, certain models of heart failure feature increased CaM³⁰. In all, exploring the physiological and pathophysiological sequelae of Ca^{2+} channel connectivity with CaM is now an important frontier of research.

METHODS SUMMARY

Molecular biology. We made channel chimaeras, mutants and CFP/YFP-tagged FRET constructs using standard molecular biological techniques. Detailed strategies for engineering various constructs are detailed in Methods.

Transfection of HEK293 cells. We transiently expressed channels in HEK293 cells using established Ca^{2+} -phosphate-based procedures^{6,8}.

Whole-cell electrophysiology. We performed whole-cell recordings in HEK293 cells at room temperature (20–22 °C) on an Axopatch 200A amplifier (Axon Instruments). The series resistance was 1–3 M Ω , before series resistance compensation of 80%. P/8 leak subtraction was used throughout. We low-pass filtered current records at 2 kHz and digitized them at rates several times greater. Detailed experimental conditions are described at length in Methods.

FRET optical imaging. We carried out FRET two-hybrid experiments in HEK293 cells and analysed them as previously described⁶. During imaging, the bath solution was either a Tyrode's buffer containing 2 mM Ca^{2+} or the standard electrophysiological-recording bath solution. Concentration-dependent spurious FRET was subtracted from the raw data before binding-curve analysis¹⁷.

Full Methods and any associated references are available in the online version of the paper at www.nature.com/nature.

Received 16 July; accepted 4 December 2009.

Published online 7 February 2010.

- Jeong, H., Tombor, B., Albert, R., Oltvai, Z. N. & Barabasi, A.-L. The large-scale organization of metabolic networks. *Nature* **407**, 651–654 (2000).
- Alseikhan, B. A., DeMaria, C. D., Colecraft, H. M. & Yue, D. T. Engineered calmodulins reveal the unexpected eminence of Ca^{2+} channel inactivation in controlling heart excitation. *Proc. Natl Acad. Sci. USA* **99**, 17185–17190 (2002).
- Xu, J. & Wu, L. G. The decrease in the presynaptic calcium current is a major cause of short-term depression at a calyx-type synapse. *Neuron* **46**, 633–645 (2005).
- Krey, J. F. & Dolmetsch, R. E. Molecular mechanisms of autism: a possible role for Ca^{2+} signaling. *Curr. Opin. Neurobiol.* **17**, 112–119 (2007).
- Yang, P. S., Mori, M. X., Antony, E. A., Tadross, M. R. & Yue, D. T. A single calmodulin imparts distinct N- and C-lobe regulatory processes to individual $\text{Ca}_v1.3$ channels. *Biophys. J. Suppl.* abstr. 1669-Plat (2007).
- Erickson, M. G., Liang, H., Mori, M. X. & Yue, D. T. FRET two-hybrid mapping reveals function and location of L-type Ca^{2+} channel CaM preassociation. *Neuron* **39**, 97–107 (2003).
- Liang, H. *et al.* Unified mechanisms of Ca^{2+} regulation across the Ca^{2+} channel family. *Neuron* **39**, 951–960 (2003).
- Yang, P. S. *et al.* Switching of Ca^{2+} -dependent inactivation of $\text{Ca}_v1.3$ channels by calcium binding proteins of auditory hair cells. *J. Neurosci.* **26**, 10677–10689 (2006).
- Black, D. J., Leonard, J. & Persechini, A. Biphasic Ca^{2+} -dependent switching in a calmodulin-IQ domain complex. *Biochemistry* **45**, 6987–6995 (2006).
- Singh, A. *et al.* Modulation of voltage- and Ca^{2+} -dependent gating of $\text{Ca}_v1.3$ L-type calcium channels by alternative splicing of a C-terminal regulatory domain. *J. Biol. Chem.* **283**, 20733–20744 (2008).
- Singh, A. *et al.* C-terminal modulator controls Ca^{2+} -dependent gating of $\text{Ca}_v1.4$ L-type Ca^{2+} channels. *Nature Neurosci.* **9**, 1108–1116 (2006).
- Wahl-Schott, C. *et al.* Switching off calcium-dependent inactivation in L-type calcium channels by an autoinhibitory domain. *Proc. Natl Acad. Sci. USA* **103**, 15657–15662 (2006).
- Platzer, J. *et al.* Congenital deafness and sinoatrial node dysfunction in mice lacking class D L-type Ca^{2+} channels. *Cell* **102**, 89–97 (2000).
- Namkung, Y. *et al.* Requirement for the L-type Ca^{2+} channel α_{1D} subunit in postnatal pancreatic β cell generation. *J. Clin. Invest.* **108**, 1015–1022 (2001).
- Strom, T. M. *et al.* An L-type calcium-channel gene mutated in incomplete X-linked congenital stationary night blindness. *Nature Genet.* **19**, 260–263 (1998).
- Doering, C. J., Hamid, J., Simms, B., McRory, J. E. & Zamponi, G. W. $\text{Ca}_v1.4$ encodes a calcium channel with low open probability and unitary conductance. *Biophys. J.* **89**, 3042–3048 (2005).
- Dick, I. E. *et al.* A modular switch for spatial Ca^{2+} selectivity in the calmodulin regulation of Ca_v channels. *Nature* **451**, 830–834 (2008).
- Peterson, B. Z. *et al.* Critical determinants of Ca^{2+} -dependent inactivation within an EF-hand motif of L-type Ca^{2+} channels. *Biophys. J.* **78**, 1906–1920 (2000).
- Griessmeier, K. *et al.* Calmodulin is a functional regulator of $\text{Ca}_v1.4$ L-type Ca^{2+} channels. *J. Biol. Chem.* **284**, 29809–29816 (2009).
- Cantor, C. R. & Schimmel, P. R. *Biophysical Chemistry: Part III: The Behavior of Biological Macromolecules* 11th edn, 887–978 (Macmillan, 1980).
- Kim, J., Ghosh, S., Nunziato, D. A. & Pitt, G. S. Identification of the components controlling inactivation of voltage-gated Ca^{2+} channels. *Neuron* **41**, 745–754 (2004).
- Xiong, L., Kleerekoper, Q. K., He, R., Putkey, J. A. & Hamilton, S. L. Sites on calmodulin that interact with the C-terminal tail of $\text{Ca}_v1.2$ channel. *J. Biol. Chem.* **280**, 7070–7079 (2005).
- Black, D. J., Tran, Q. K. & Persechini, A. Monitoring the total available calmodulin concentration in intact cells over the physiological range in free Ca^{2+} . *Cell Calcium* **35**, 415–425 (2004).
- Slemmon, J. R., Feng, B. & Erhardt, J. A. Small proteins that modulate calmodulin-dependent signal transduction: effects of PEP-19, neuromodulin, and neurogranin on enzyme activation and cellular homeostasis. *Mol. Neurobiol.* **22**, 99–113 (2000).
- Chambers, J. S., Thomas, D., Saland, L., Neve, R. L. & Perrone-Bizzozero, N. I. Growth-associated protein 43 (GAP-43) and synaptophysin alterations in the dentate gyrus of patients with schizophrenia. *Prog. Neuropsychopharmacol. Biol. Psychiatry* **29**, 283–290 (2005).
- Bezprozvanny, I. Calcium signaling and neurodegenerative diseases. *Trends Mol. Med.* **15**, 89–100 (2009).
- Maslah, E. *et al.* Dopaminergic loss and inclusion body formation in α -synuclein mice: implications for neurodegenerative disorders. *Science* **287**, 1265–1269 (2000).
- Lee, D., Lee, S. Y., Lee, E. N., Chang, C. S. & Paik, S. R. α -Synuclein exhibits competitive interaction between calmodulin and synthetic membranes. *J. Neurochem.* **82**, 1007–1017 (2002).
- Chan, C. S. *et al.* 'Rejuvenation' protects neurons in mouse models of Parkinson's disease. *Nature* **447**, 1081–1086 (2007).
- Ikeda, S. *et al.* MicroRNA-1 negatively regulates expression of the hypertrophy-associated calmodulin and Mef2a genes. *Mol. Cell. Biol.* **29**, 2193–2204 (2009).

Supplementary Information is linked to the online version of the paper at www.nature.com/nature.

Acknowledgements We thank M. Tadross, I. Dick and members of the Calcium Signals Laboratory for comments; M. Tadross for data-acquisition software; D. J. Black and A. Persechini for BSCaM_{IQ} and neuromodulin complementary DNA; J. McRory and T. Snutch for human α_{1F} cDNA; J. Streissnig for human α_{1D} cDNA; and V. Wu for earlier foundational experiments. This work is supported by grants from the US National Institute of Mental Health, the US National Heart, Lung, and Blood Institute and the US National Institute of Neurological Disorders and Stroke.

Author Contributions X.L. devised and refined experimental design, carried out all phases of the experiments and performed extensive data analysis. P.S.Y. consulted on initial molecular biology approaches, constructed certain channels with ICDI point mutations and contributed importantly to $\text{Ca}_v1.4$ expression strategies and electrophysiological characterization. W.Y. conducted FRET experiments, undertook molecular biology and extensively managed technical aspects of the project. D.T.Y. conceived, refined and oversaw the experiments, performed FRET experiments, analysed data and wrote the manuscript. All authors commented on and edited the manuscript.

Author Information Reprints and permissions information is available at www.nature.com/reprints. The authors declare no competing financial interests. Correspondence and requests for materials should be addressed to D.T.Y. (dyue@jhmi.edu).

METHODS

Molecular biology. We engineered the rat $\text{Ca}_v1.3$ long variant (α_{1D} , AF370009.1) as follows. For Fig. 1, a unique XbaI site was introduced by PCR following the IQ domain. The DCT of human α_{1F} (NP005174) was amplified and cloned non-directionally via the unique XbaI site, yielding the sequence in Supplementary Information, section 1.1. For Supplementary Fig. 3.4, a similar process was performed, except appropriate sections of the DCT of rat $\text{Ca}_v1.3$ long variant (α_{1D} , AF370009.1) were first PCR amplified with flanking SpeI and XbaI sites (compatible ends) and cloned into the aforementioned unique XbaI site, leaving a unique XbaI site after the inserted section of the rat DCT. Appropriate segments of the ICDI segment of the human $\text{Ca}_v1.3$ long variant (α_{1D} , NM000718) were then PCR-amplified with flanking SpeI and XbaI sites and cloned into the unique XbaI site, leaving a unique XbaI site after the inserted ICDI segment. For the V41A insertion (Supplementary Fig. 3.4d), the human ICDI was point mutated using QuikChange mutagenesis (Stratagene) before PCR amplification and insertion into the channel construct. For the A41V insertion (Supplementary Fig. 3.4e), the rat ICDI was similarly point-mutated before cloning into the unique XbaI site of the aforementioned engineered rat $\text{Ca}_v1.3$ long variant. For FRET two-hybrid constructs, fluorophore-tagged CaM constructs were made as described previously⁶. We made other FRET constructs by replacing CaM with appropriate PCR-amplified segments, via unique NotI and XbaI sites flanking CaM⁶. Details of CaM sponges can be found in Supplementary Information, section 3.1. All segments subject to PCR or QuikChange were verified in their entirety by sequencing.

Transfection of HEK293 cells. For electrophysiology experiments, HEK293 cells were cultured in 10-cm plates, and channels were transiently transfected following a calcium phosphate protocol^{6,8}. We applied 8 μg of cDNA encoding the α_1 subunit of the desired channel, along with 8 μg of rat brain β_{2a} subunit (M80545) and 8 μg of rat brain $\alpha_{2\delta}$ subunit (NM012919.2). β_{2a} minimized voltage inactivation, enhancing resolution of CDI. Additional cDNA was added as required

in co-transfections. All of the above cDNA constructs were driven by a cytomegalovirus promoter. To enhance expression, cDNA for simian virus 40 T antigen (1–2 μg) was co-transfected. For FRET two-hybrid experiments, transfections and experiments were performed as described previously⁶. Electrophysiology and FRET were done at room temperature (20–22 °C) 1–2 days after transfection.

Whole-cell recording. Whole-cell recordings were obtained at room temperature using an Axopatch 200A amplifier (Axon Instruments). Electrodes were pulled with borosilicate glass capillaries (MTW 150-F4, World Precision Instruments), resulting in 1–3-M Ω resistances, before series resistance compensation of 80%. The internal solutions contained 135 mM CsMeSO₃, 5 mM CsCl₂, 1 mM MgCl₂, 4 mM MgATP, 5 mM HEPES (pH 7.3) and 5 mM EGTA, at 290 mosM, adjusted with glucose. The bath solution contained 140 mM TEA-MeSO₃, 10 mM HEPES (pH 7.3) and 10 mM CaCl₂ or BaCl₂, at 300 mosM, adjusted with glucose. These are as reported previously⁸. To augment currents for the full-length $\text{Ca}_v1.4$ experiments in Fig. 2e, we used 40 mM CaCl₂ or BaCl₂ in the bath solution and adjusted TEA-MeSO₃ downwards to preserve osmolarity. Furthermore, 5 μM Bay K 8644 was present in the bath throughout to further enhance currents.

FRET optical imaging. FRET two-hybrid experiments were carried out in HEK293 cells and analysed as described previously⁶. During imaging, the bath solution was either a Tyrode's buffer containing 2 mM Ca²⁺ or the standard electrophysiological-recording bath solution described earlier. Concentration-dependent spurious FRET was subtracted from the raw data before binding-curve analysis¹⁷. For simultaneous BSCaM_{IQ} imaging and patch-clamp recording, three-cube FRET measurements were obtained before whole-cell break-in, and did not change appreciably thereafter. For ICDI binding curves in Figs 2a and 4b, an unlabelled IQ domain of neuromodulin (see Supplementary Information, section 3.1, for sequence) was co-expressed to reduce interference from endogenous CaM.

1. Additional data for Fig. 1

1.1. Detailed specification of constructs

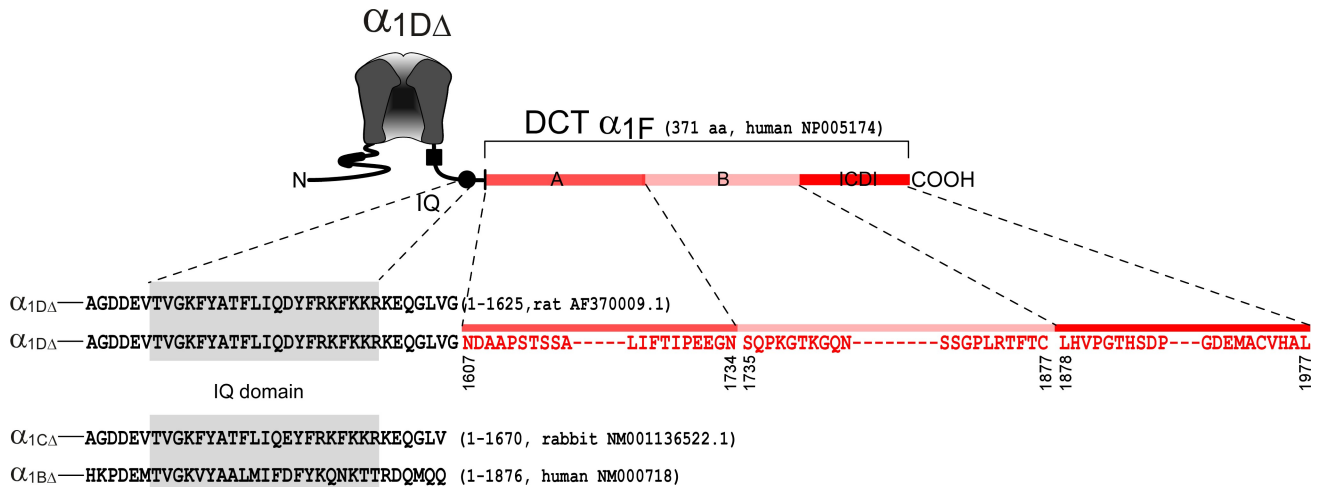


Fig. S1.1 Detailed sequence information for constructs used in Fig. 1, and affiliated supplemental information. In addition to α_1 subunits, we co-transfected auxiliary β_{2a} (M80545) and $\alpha_2\delta$ (NM012919.2) subunits throughout. Versions of $\alpha_{1C\Delta}$ and $\alpha_{1B\Delta}$ were appended to the DCT of α_{1F} as well. Accession numbers in parentheses. The DCT region was cloned non-directionally via a unique Xba I site, introducing an SR.

1.2. $\text{Ca}_v1.2$ channel CDI is decreased by the DCT of α_{1F}

Adding the $\text{Ca}_v1.4$ DCT to the $\text{Ca}_v1.2$ channel core (Figs. S1.2) also attenuated CDI. Panel **a** shows the CDI profile of the core $\text{Ca}_v1.2$ channel (Fig. S1.1 details the composition), with the display format identical to that in main text Fig. 1, except that reference depolarizations are to +10 mV, and bar graphs report the population data for inactivation metrics. Panel **b** displays the decrease, but not elimination of CDI seen upon addition of the DCT.

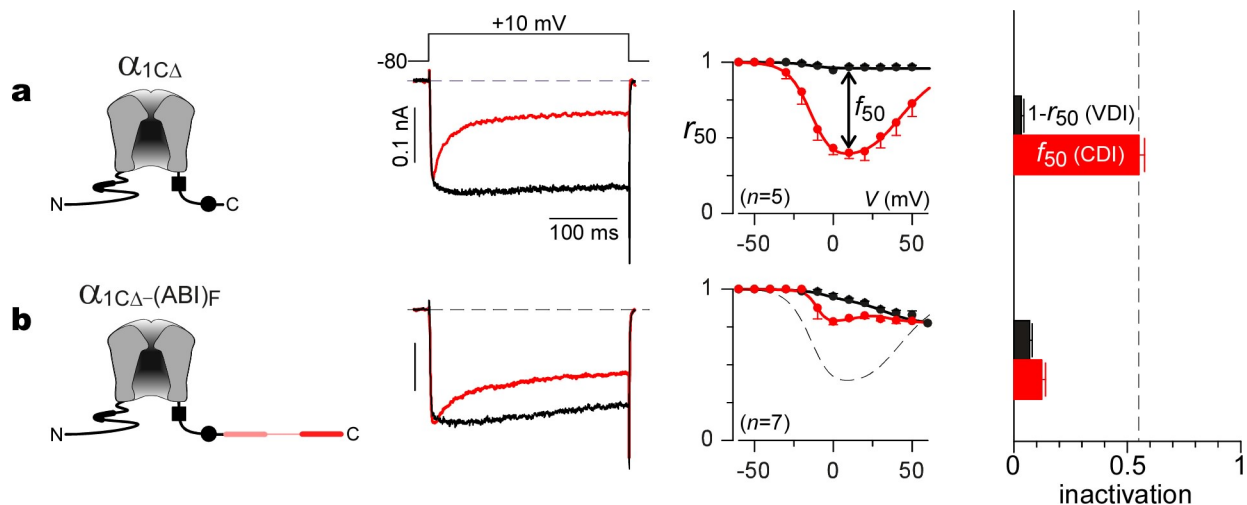


Fig. S1.2 Effects of the DCT of α_{1F} upon CDI in $\text{Ca}_v1.2$ channels. **a**, Behavior of core $\text{Ca}_v1.2$ channels. $1 - r_{50}$ is a metric for the strength of voltage-dependent inactivation (VDI). **b**, DCT of α_{1F} attenuates CDI of $\text{Ca}_v1.2$. Dashes reproduce Ca^{2+} profile from panel **a**. **a** and **b**, Format as in main text Fig. 1, except exemplar currents at 10 mV. Red bars show f_{50} values. Black bars show $1 - r_{50}$ values for Ba^{2+} current.

1.3. Cav2.2 channel CDI is unaffected by the DCT of α_{1F}

By contrast to experiments with core channels comprised of Cav1 subunits (main text Fig. 1, Supplemental Fig. S1.2), appending the DCT of α_{1F} does *not* diminish CDI of core channels comprised of the main Cav2.2 subunit (α_{1B}). Fig. S1.3a summarizes the baseline CaM-mediated CDI of a core Cav2.2 channel⁵, which incorporates the pore-forming $\alpha_{1B\Delta}$ subunit (defined above in Fig. S1.1). The format is identical to that in main text Fig. 1, except that 300-msec metrics are used to accommodate the slower CDI kinetics typical of these channels. Fig. S1.3b demonstrates that CDI is no different upon appending the DCT of α_{1F} . Thus, the DCT of α_{1F} requires complementary elements within the channel core, in order to reduce CDI. Those elements are presumably lacking in the Cav2.2 core.

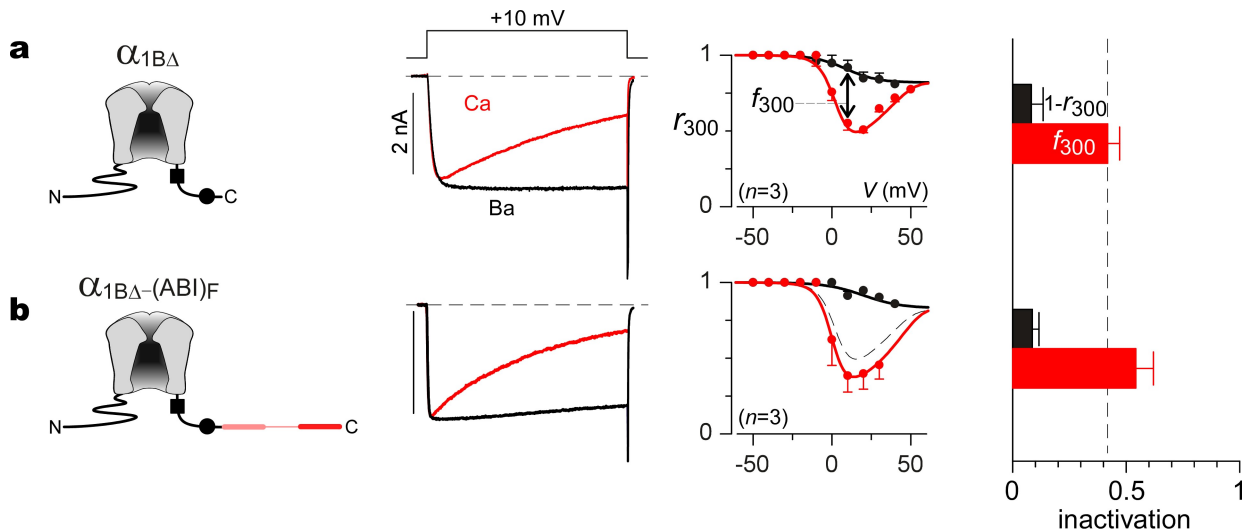


Fig. S1.3 DCT of α_{1F} does not diminish CDI of core channels comprised of the Cav2.2 pore-forming subunit ($\alpha_{1B\Delta}$). **a**, Baseline CDI. $1 - r_{300}$ is a metric for the strength of voltage-dependent inactivation (VDI). 300-msec metric used here to account for slower inactivation kinetics of N-type channel core. **b**, CDI upon appending the DCT of α_{1F} . Control metrics from **a** reproduced for reference. Patch solutions identical to those used for Cav1.3, except internal Ca^{2+} buffering now 0.5 mM EGTA, to allow for global Ca^{2+} selectivity of CDI within

1.4. Segment A and ICDI module of DCT of α_{1F} are functionally critical

To establish which elements within the DCT of α_{1F} were functionally critical for the attenuation of CDI, we performed additional deletion analysis of the $\alpha_{1D\Delta}$ -(ABI)_F construct in main text Fig. 1b. Fig. S1.4 summarizes the results, following the identical format to main text Fig. 1b, the average results of which are reproduced at the top for reference. Deleting the A region from the DCT rendered this module incapable of attenuating CDI (Fig. S1.4b); hence, the A segment is functionally critical. By contrast, deleting the B region from the DCT fully spared the module's ability to blunt CDI, yielding CDI attenuation equal to that seen with the entire DCT (Fig. S1.4c). Hence, the B region is functionally irrelevant. Deleting both A and B regions, leaving only the ICDI region, rendered the DCT module largely inactive (Fig. S1.4d), sparing a small decrement of CDI compared to core channels. Thus, while the ICDI element alone is capable of some effect, it requires the A segment for full activity. Finally, truncating the first 40 residues from the ICDI element in the $\alpha_{1D\Delta}$ -(AI)_F construct of Fig. S1.4c, entirely eliminates the DCT effect in the $\alpha_{1D\Delta}$ -(AI)₄₁₋₁₀₀_F construct in Fig. S1.4e. Hence, at least part of the ICDI is critical. In all, both A and ICDI elements are necessary for DCT function.

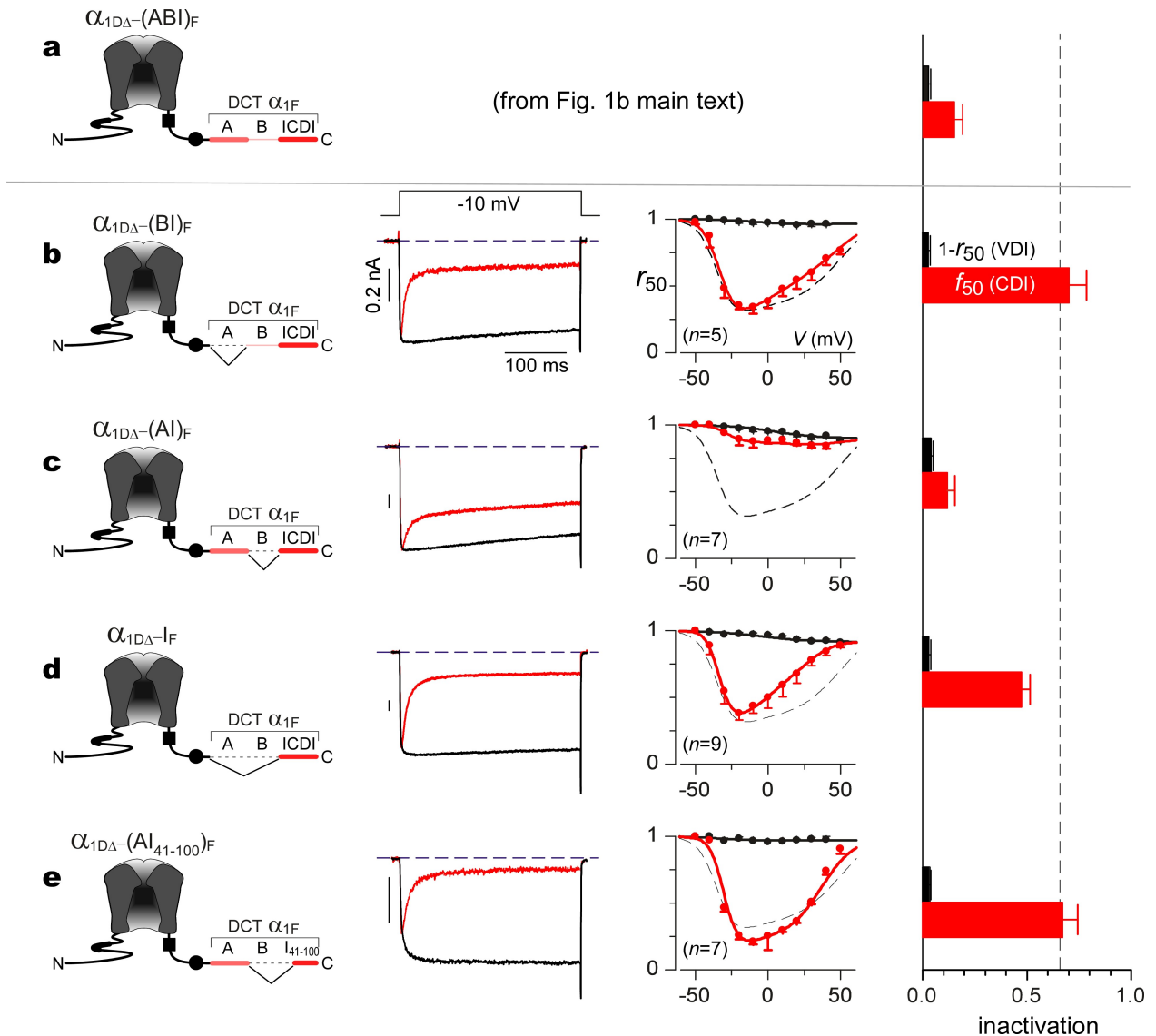


Fig. S1.4 Deletion analysis of the α_{1DA} -(ABI)_F construct. Format as in main text Fig. 1 throughout this supplemental figure. **a**, Summary of CDI profile of α_{1DA} -(ABI)_F construct, copied from main text Fig. 1b for reference. Bar graphs indicate strongly attenuated CDI, compared to that of core channels whose behavior follows the dashed curves. **b**, Deleting the A segment fully restores CDI. **c**, Deleting the B region fully maintains suppression of CDI by the remaining DCT elements. **d**, Deleting both A and B segments, leaving only the ICDI element, yields only a small decrease of CDI. **e**, Deleting the first 40 aa of the ICDI element in the construct of panel **c** (leaving VALA . . . VHAI) fully eliminates DCT function. Sequences in Fig. S1.1; QuikChange used to delete DCT portions, before non-directional cloning into a unique Xba I site.

1.5. Competitive versus strict allosteric mechanisms underlying DCT effects

There is an ongoing controversy concerning the mechanism underlying DCT effects. One proposed mechanism is the strict allosteric scheme diagrammed in Fig. S1.5a. Here, the ICDI module leaves apoCaM/channel binding unchanged, but the association of ICDI with an EF-hand-like module eliminates CDI transduction. Alternatively, in a competitive mechanism as shown in Fig. S1.5b, ICDI competes with apoCaM for binding near the channel IQ domain. CDI is thus inhibited by displacement of CaM from channels.

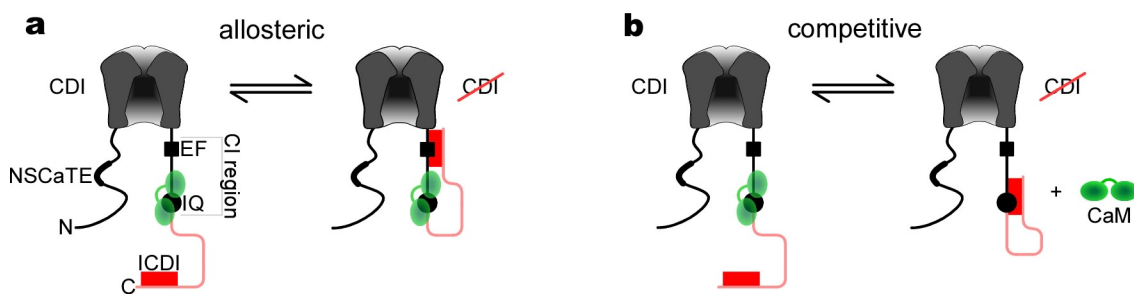


Fig. S1.5 Two proposed mechanisms underlying DCT effects. **a**, Strict allosteric mechanism. ICDI binding to EF-hand-like module does not perturb apoCaM binding to IQ domain, but instead eliminates transduction of CDI. **b**, Competitive inhibitory mechanism. ICDI competes with apoCaM for binding to IQ domain. Channels fail to undergo CDI because they altogether lack a preassociated apoCaM.

2. Additional data for Fig. 2

2.1. Detailed composition of FRET 2-hybrid constructs

For main text Figs. 2a through 2c, EYFP–PreIQ₃–IQ_D–A_F contains the PreIQ₃–IQ_D segment of the rat $\alpha_{1D\Delta}$ subunit (IKTEGNLEQANEELRAVIKIKIWKKTSMKLLDQVVPVPPAGDDEVTVGKIFYAFLIQ...GLVG) fused to the A segment of α_{1F} in Fig. S1.1. CFP–CaM_{WT} is as published³. For main text Figs. 2d and 2e, CaM_{WT} and CaM sponge (specifically, EYFP–PreIQ₃–IQ of α_{1C}) are also as published³.

2.2. Additional FRET interactions of the ICDI element of α_{1F}

To confirm that the FRET interactions in main text Fig. 2c are representative of those pertaining to full-length Cav1.4 channels, Fig. S2.2a shows the FRET binding curve for the apoCaM preassociation domain of Cav1.4 (EYFP–PreIQ₃–IQ_F–A_F) with ECFP–ICDI_F. This curve is closely similar to that for interacting partners of the $\alpha_{1D\Delta}$ –(ABI)_F channel chimera in main text Fig. 2c, suggesting that this chimera is an appropriate proxy for full-length Cav1.4 behavior.

Structural modeling and electrophysiological analysis of Cav1.2 channel deletions/mutations indirectly suggest that segments homologous to the A and ICDI segments bind in these channels⁷. Moreover, single-metric FRET analysis of homologous A and ICDI segments in Cav1.3 channels also indirectly suggest that these segments interact⁸. By contrast, our FRET 2-hybrid analysis below (Fig. S2.2b) directly indicates a lack of FRET interaction between A and ICDI segments of the DCT of Cav1.4 channels, over a wide range of free ICDI concentrations. Instead of direct interaction, the A region is important to permit the PreIQ₃–IQ domain to interact well with the ICDI region (not shown).

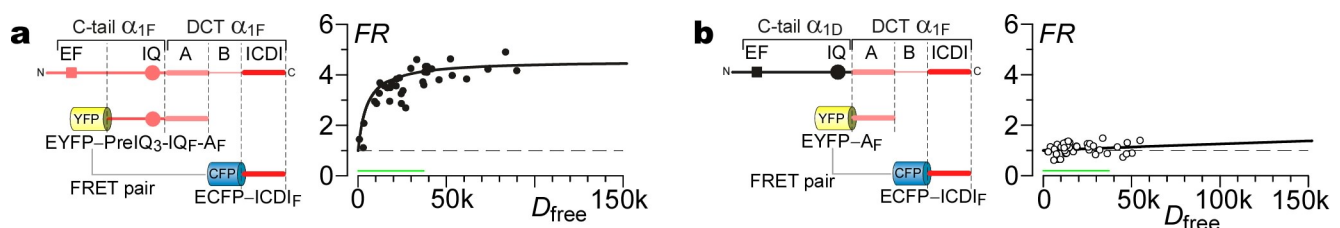


Fig. S2.2 **a**, FRET 2-hybrid binding curve for EYFP–PreIQ₃–IQ_F–A_F and ECFP–ICDI_F, all derived from Cav1.4. **b**, A and ICDI elements of α_{1F} (main pore-forming subunit of Cav1.4 channels) fail to exhibit FRET interaction. Failure of data points to rise above unity indicates lack of appreciable FRET interaction. **a** and **b**, Format identical to that in main text Fig. 2a. Left, schematic of FRET partners used in experiment. Right, binding curve plotting *FR* metric of FRET (proportional to FRET efficiency) versus relative concentration of free ICDI species.

2.3. Overexpression of Ca^{2+} insensitive mutant CaMs with $\alpha_{1D\Delta}$ -(ABI)_F construct

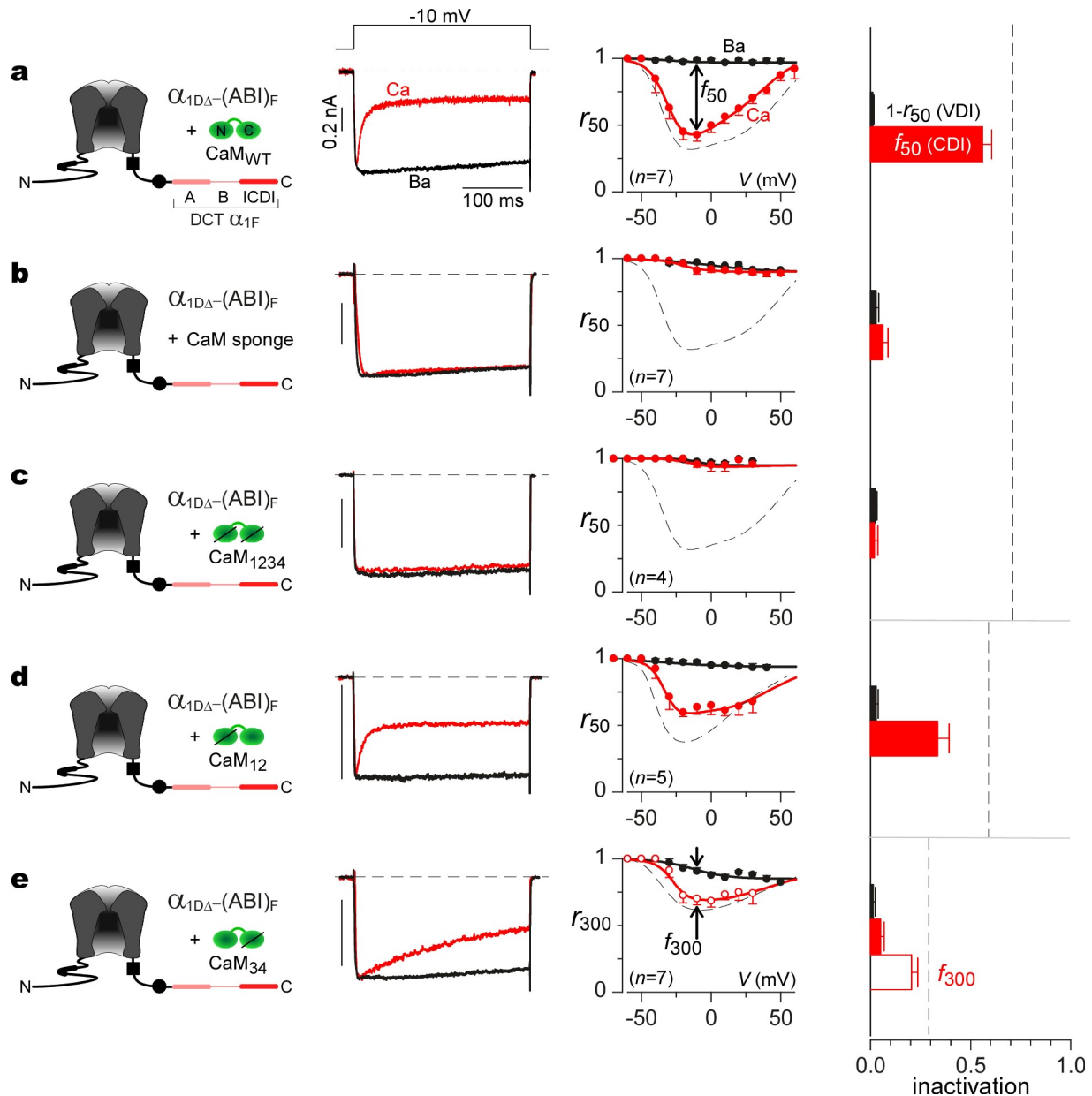


Fig. S2.3 Changes in the CDI of $\alpha_{1D\Delta}$ -(ABI)_F channels upon manipulating wild-type CaM levels, or overexpressing various Ca^{2+} -sensitive mutant CaM molecules¹. Format as in main text Fig. 1, with addition of bar graph population summaries of voltage-dependent inactivation (VDI) and CDI parameters at far right. **a, b**, Expanded analysis of main text Fig. 2d. **a**, Overexpressing wild-type CaM restores CDI almost to control levels (dashes). **b**, Chelating CaM with a CaM sponge peptide nearly eliminates CDI. **c**, Coexpression with CaM₁₂₃₄ eliminates all appreciable CDI. **d**, Coexpression with CaM₁₂ largely restores a C-lobe form of CDI. Dashed curves show metrics for parallel experiments on Ca_v1.3 channels lacking a DCT⁴. **e**, Coexpression with CaM₃₄ largely restores an N-lobe form of CDI. Dashed curves show metrics for parallel experiments on Ca_v1.3 channels lacking a DCT⁴. Additional 300-msec CDI metrics used here to facilitate characterization of slower N-lobe form of CDI.

Co-expressing the $\alpha_{1D\Delta}$ -(ABI)_F construct with an abundance of CaM and CaM sponges (Figs. S2.3a and S2.3b, respectively)—or with a plethora of various Ca^{2+} -sensitive mutant CaM molecules¹ (Figs. S2.3c through S2.3e)—all furnish another body of evidence that circumstantially supports a competitive inhibitory mechanism (Fig. S1.5b). For panels a and b, these data sets amplify the analysis shown in main text Fig. 2d. Alternatively, if we could fully repopulate channels with a specific form of mutant CaM under a competitive inhibitory mechanism (panels c through e), then the resulting CDI profile should adopt

that of channels that lack a DCT module and bear such mutant CaM molecules⁴. Indeed, this outcome is largely realized. When a CaM lacking Ca²⁺ binding to all four EF hands (CaM₁₂₃₄) is coexpressed, CDI becomes essentially zero (Fig. S2.3c). When a CaM₁₂ (Ca²⁺ binding only to C-lobe of CaM) is coexpressed, a mostly C-lobe form of CDI is observed (Fig. S2.3d). CDI metrics for C-lobe CDI in channels lacking a DCT are shown as dashed relations⁴. When CaM₃₄ is coexpressed, a mostly N-lobe form of CDI is observed (Fig. S2.3e). Here, 300-msec CDI metrics are included, to resolve the slow N-lobe form of CDI with better precision. Dashed relations indicate the N-lobe CDI metrics from channels lacking a DCT element⁴. The close approximation of $\alpha_{1D\Delta}$ -(ABI)_F data with that of Cav1.3 lacking a DCT module circumstantially supports a competitive inhibitory mechanism.

3. Formulation of Equation 1 for competitive inhibitory mechanism in Fig. 3

3.1. Sequence of CaM sponges in Fig. 3b

Filled green symbol, rat neuromodulin IQ domain⁶ (MAATKIQA^AFRGHITRKKLKDEKKGASRGPYSIVSPKC, NP058891), with boldface S41A mutation to eliminate PKC site⁶; open symbol, PreIQ3-IQ of α_{1C} as reported³; both without fluorophore.

3.2. FR to apoCaM relation

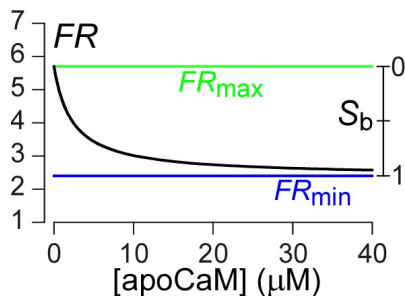


Fig. S3.2 Relation between FRET metric³ FR and free apoCaM concentration, as given by the BSCaM_{IQ} sensor in HEK293 cells⁶. FR relates to the fractional binding of BSCaM_{IQ} with apoCaM by the following equation: $S_b = (FR_{max} - FR) / (FR_{max} - FR_{min})$, where FR_{max} and FR_{min} values are given by green and blue line levels. Green and blue lines identical to those in main text Fig. 3b. Free apoCaM concentration is then determined from S_b via Eq. S4 below. Plotting these relations yields the black curve shown at left that relates FR to free apoCaM concentration.

3.3. Derivation in terms of BSCaM_{IQ} sensor readouts

From previous analyses, we know that channels lacking a preassociated apoCaM fail to exhibit CDI^{3,5}. Additionally, a competitive inhibitory mechanism postulates that once apoCaM preassociates with the channel to displace the competitive inhibitor (ICDI), the strength of CDI (f_{50} , as defined in main text Fig. 1a) should adopt the full value CDI_{max} , just as observed without inhibitor⁹. Accordingly, according to this model, the strength of CDI is

$$CDI = CDI_{max} \cdot F_{bound-channel} + 0 \cdot (1 - F_{bound-channel}) \quad (S1)$$

where $F_{bound-channel}$ is the fraction of channels to which apoCaM is pre-bound. Ca²⁺ binding to pre-bound apoCaM then drives conformational changes that invoke CDI. This equation also presumes that channels preassociated with apoCaM exhibit the same single-channel current amplitudes as do channels without CaM. These and other presumptions will ultimately be confirmed by full consistency with extensive data sets within the main text.

According to a competitive inhibitory mechanism, we can also postulate that

$$F_{bound-channel} = \frac{[apoCaM]}{[apoCaM] + K_{d-channel-apparent}} \quad (S2)$$

where $[apoCaM]$ is the free concentration of apoCaM, and $K_{d-channel-apparent}$ is the apparent dissociation constant of the channel in the presence of a fixed concentration of inhibitor (as true with an ICDI element covalently linked to the channel complex). This equation exploits the facts that CaM exchanges slowly with Ca²⁺ channels over the course of ~30 minutes¹⁰, and that our culture conditions and experiments maintain cells in the resting state where apoCaM predominates^{3,11}, except for brief activations of channel current in the presence of 5 mM intracellular EGTA (which maintains all but local Ca²⁺ concentration near zero). These periods of activation do not perturb $F_{bound-channel}$, as repeated cycles of activation fail to appreciably change CDI (see Eq. S1).

To link these equations to FRET sensor readings, we recall that the BSCaM_{IQ} sensor gives direct measurements of [apoCaM] according to⁶

$$S_b = \frac{[\text{apoCaM}]}{[\text{apoCaM}] + K_{d\text{-sensor}}} \quad (\text{S3})$$

where S_b is the fraction of sensor bound to apoCaM (readout from Fig. S3.2 and main text Fig. 3b), and $K_{d\text{-sensor}}$ is the dissociation constant of the sensor in HEK293 cells, determined to be 2.3 μM ⁶. The accuracy of this description of the sensor is enhanced for several reasons. The BSCaM_{IQ} sensor is sensitive almost exclusively to free apoCaM concentration (not $\text{Ca}^{2+}/\text{CaM}$), unless Ca^{2+} is elevated to far greater than 10 μM ⁶. Readings of the sensor are taken in resting HEK293 cells (before whole-cell dialysis is begun), where the Ca^{2+} is certainly less than 10 μM . The whole-cell recording solution contains 5 mM EGTA to ensure near zero global Ca^{2+} upon dialysis, so that sensor readings do not change appreciably upon whole-cell recording and activation of currents. Also, the nearly constant FRET upon dialysis also suggests negligible CaM diffusion from cell to pipet over ~ 10 m recording.

As FRET measurements furnish a direct determination of S_b , as diagrammed in main text Fig. 3b, it is useful to convert Eq. S3 into a determination of [apoCaM] in terms of S_b .

$$[\text{apoCaM}] = K_{d\text{-sensor}} \cdot \frac{S_b}{1 - S_b} \quad (\text{S4})$$

Substituting Eq. S4 into S2 yields

$$F_{\text{bound-channel}} = \frac{K_{d\text{-sensor}} \cdot \frac{S_b}{1 - S_b}}{K_{d\text{-sensor}} \cdot \frac{S_b}{1 - S_b} + K_{d\text{-channel-apparent}}} \quad (\text{S5})$$

Substituting Eq. S5 into Eq. S1 then yields Eq. 1 in the main text.

3.4. Exemplar current traces for Figs. 3e through 3g

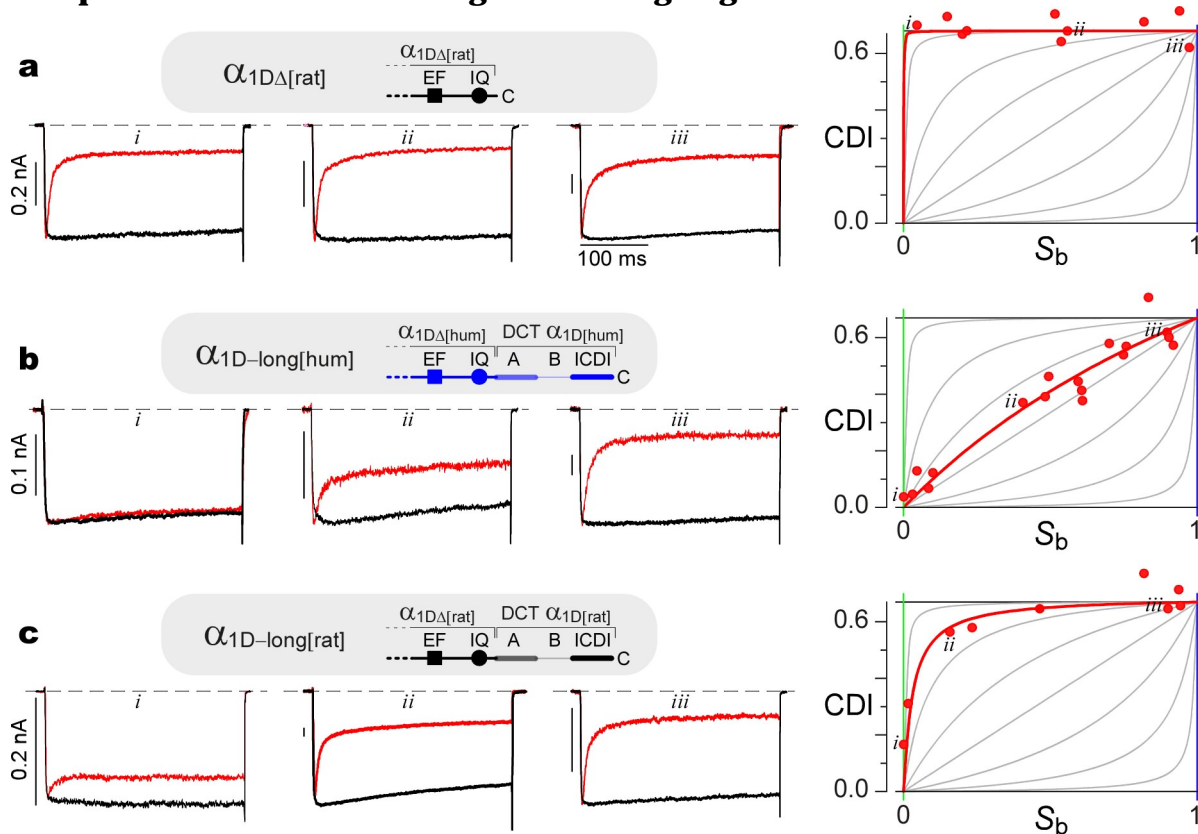


Fig. S3.4 Exemplar currents accompanying main text Figs. 3e, 3f, and 3g. **a**, Reproduction of main text Fig. 3e graph for $\alpha_{1D\Delta}[\text{rat}]$ (far right), now labelled with exemplar current labels (i – iii). The corresponding exemplar currents are displayed at left. **b**, Reproduction of main text Fig. 3f data for $\alpha_{1D\text{-long}}[\text{hum}]$ (far right); affiliated exemplar currents (left). Format as in **a**. **c**, Reproduction of main text Fig. 3g data for $\alpha_{1D\text{-long}}[\text{rat}]$ (far right); affiliated exemplar currents (left). Format as in **a**.

3.5. Single-residue switch explains differing ICDI functions of rat versus human Cav1.3

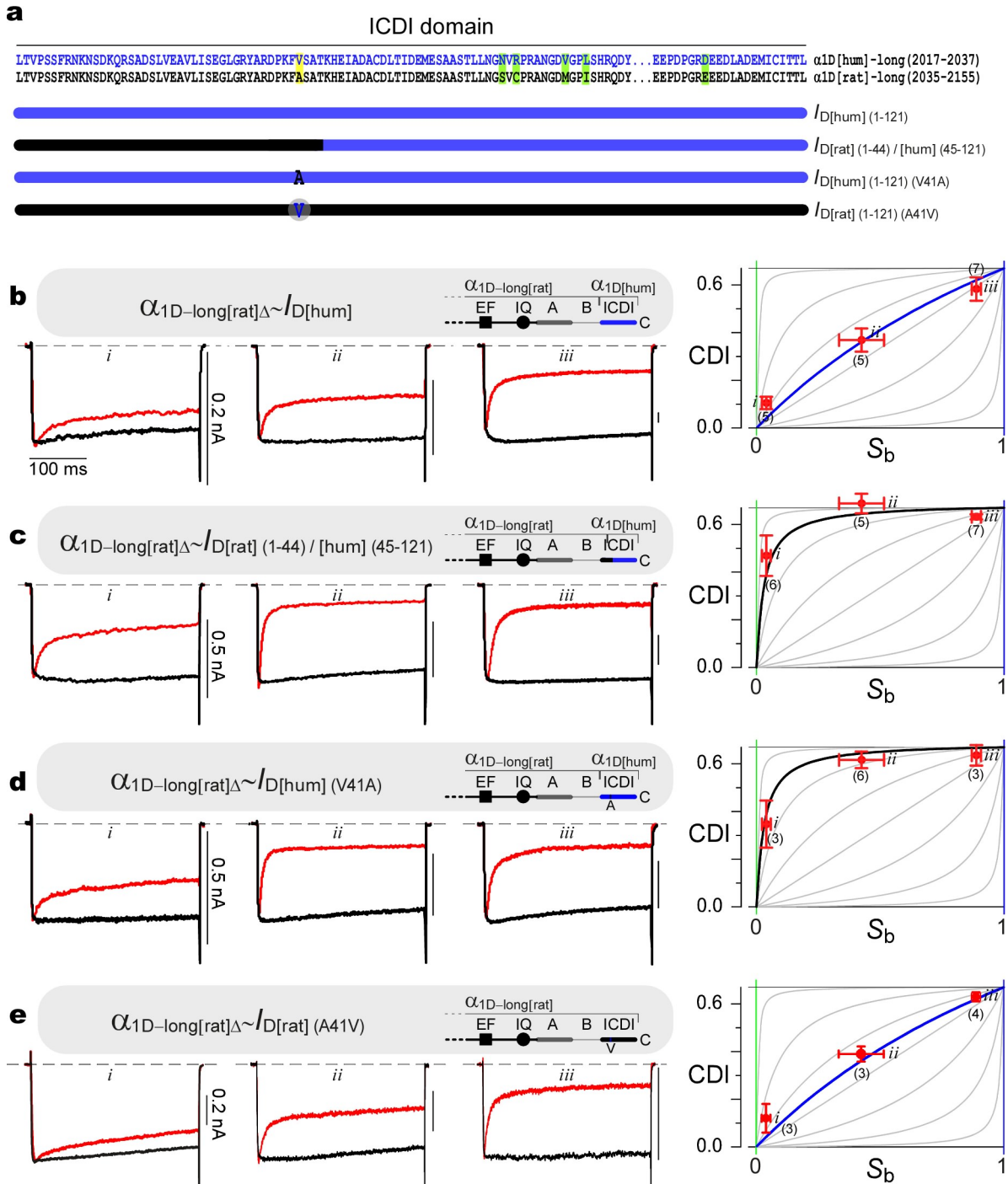


Fig. S3.5 Single residue differentially tunes long variants of human and rat Cav1.3. **a**, Amino-acid alignments of ICDI region for long variants of human and rat Cav1.3. Top, highlighted residues mark differences between variants; bottom, bars schematize engineered versions of ICDI to be substituted into $\alpha_{1D\text{-long[rat]}}$ below. An SS punctuates IQ/A and rat/human junctions in these constructs. **b**, $CDI-S_b$ analysis for $\alpha_{1D\text{-long[rat]}\Delta\sim I_{D[\text{hum}]}$ (human ICDI substituted into the long rat variant) converts the rat into human phenotype. **c**, $CDI-S_b$ analysis for $\alpha_{1D\text{-long[rat]}\Delta\sim I_{D[\text{rat}] (1-44) / [\text{hum}] (45-121)}$ (last 77 residues of human ICDI substituted into the rat variant) shows sparing of the rat profile, implicating functional dominance of first 44 residues in human ICDI. **d**, $CDI-S_b$ analysis for $\alpha_{1D\text{-long[rat]}\Delta\sim I_{D[\text{hum}] (V41A)}$ (human ICDI with V41A mutation substituted into rat variant) spares the rat profile, identifying a valine-to-alanine switch at ICDI position 44 as critical to intra-species tuning of long Cav1.3 variants. **e**, $CDI-S_b$ analysis for $\alpha_{1D\text{-long[rat]}\Delta\sim I_{D[\text{rat}] (A41V)}$ (rat ICDI with A41V mutation substituted into rat variant) confers the human profile, proving the valine-to-alanine switch at ICDI position 44 to be both necessary and sufficient for the intra-species tuning of long Cav1.3 variants.

Given that ICDI peptide interactions presumably underlie channel inhibitory tuning (main text Fig. 2c), we focused a search for critical residues within this locus. Upon substituting the human Cav1.3 ICDI element ($I_{D[hum]}(1-121)$, Fig. S3.5a) into the long variant of rat Cav1.3 channels, the resulting channels exhibited a $CDI-S_b$ profile approximating that of the long Cav1.3 variant of humans (Fig. S3.5b, blue curve from main text Fig. 3f), confirming functional dominance of ICDI. An abbreviated $CDI-S_b$ analysis was employed to facilitate structure-function analysis (for details, see paragraph below). Upon reversion of the first 44 residues of the human ICDI into those of their rat counterpart ($I_{D[rat]}(1-44) / [hum](45-121)$, Fig. S3.5a), the $CDI-S_b$ profile resembled that of the long Cav1.3 variant of rat (Fig. S3.5c, black curve from main text Fig. 3g), demonstrating the critical nature of this initial segment. Close inspection of sequence within this zone (Fig. S3.5a) revealed a single valine (human) to alanine (rat) difference (yellow highlight). After point valine-to-alanine mutation of the human ICDI ($I_{D[hum]}(1-121)(V41A)$, Fig. S3.5a), substitution of this element into the long variant of rat Cav1.3 channels retained the $CDI-S_b$ profile of the long rat variant (Fig. S3.5d). Conversely, after point alanine-to-valine mutation of the rat ICDI ($I_{D[rat]}(1-121)(A41V)$, Fig. S3.5a), substitution of this element into the long variant of rat Cav1.3 channels conferred the $CDI-S_b$ profile of the long human variant (Fig. S3.5e). FRET assays of corresponding ICDI peptide and IQ domain binding showed directionally consistent changes in affinity (Supplemental Fig. S3.6 below). Hence, a single-residue switch gives rise to the differing inhibitory strengths of ICDI modules from rat and human Cav1.3.

Abbreviated $CDI-S_b$ analysis. To facilitate rapid structure-function analysis, S_b in these experiments were determined in separate experiments from those used to determine CDI. The lowest S_b value was obtained from $\alpha_{1D-long[hum]}$ experiments wherein overexpression of BSCaM_{IQ} was employed to chelate apoCaM (main text Fig. 3f, 5 cells). The intermediate S_b value was obtained from $\alpha_{1D\Delta}-(ABI)_F$ experiments without further apoCaM perturbation (main text Fig. 1b, 7 cells), projected through our highest resolution $CDI-S_b$ relation (main text Fig. 3d). The highest S_b value was obtained from $\alpha_{1D-long[hum]}$ experiments wherein overexpression of CaM_{WT} was employed to elevate apoCaM (main text Fig. 3f, 4 cells).

FRET 2-hybrid peptide interaction assays (Supplemental Fig. S3.6) confirm directionally consistent changes in binding of PreIQ₃-IQ-A to ICDI peptides, corresponding to $CDI-S_b$ data in Supplemental Figs. S3.5b and S3.5d.

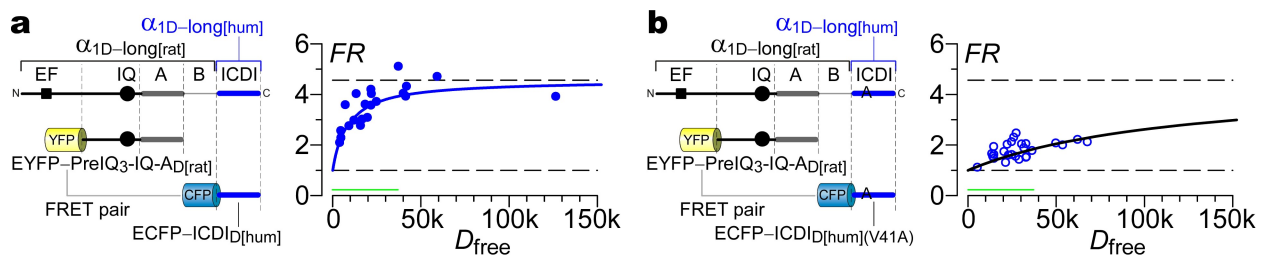


Fig. S3.6 FRET 2-hybrid analysis of peptide segments corresponding to Supplemental Figs. S3.5b, d. Format as in main text Fig. 2a, but without unlabelled neuromodulin IQ. **a**, YFP-tagged PreIQ₃-IQ-A segment of $\alpha_{1D-long[rat]}$ pitted against CFP-tagged ICDI segment of $\alpha_{1D-long[hum]}$. Binding curve data (symbols) conform to fit obtained from YFP-tagged PreIQ₃-IQ-A segment of $\alpha_{1D-long[hum]}$ pitted against CFP-tagged ICDI segment of $\alpha_{1D-long[hum]}$, reproduced from main text Fig. 4b (top). This outcome fits nicely with concordance of functional $CDI-S_b$ data between $\alpha_{1D-long[rat]}\Delta\sim I_{D[hum]}$ (Fig. S3.5b) and $\alpha_{1D-long[hum]}$ (main text Fig. 3f). **b**, YFP-tagged PreIQ₃-IQ-A segment of $\alpha_{1D-long[rat]}$ pitted against CFP-tagged ICDI segment of $\alpha_{1D-long[hum]}(V41A)$. Binding curve data (symbols) conform to fit obtained from YFP-tagged PreIQ₃-IQ-A segment of $\alpha_{1D-long[rat]}$ pitted against CFP-tagged ICDI segment of $\alpha_{1D-long[rat]}$, reproduced here from main text Fig. 4b (bottom). This outcome concurs with agreement of functional $CDI-S_b$ data of $\alpha_{1D-long[rat]}\Delta\sim I_{D[hum]}(V41A)$ (Fig. S3.5d) and $\alpha_{1D-long[rat]}$ (main text Fig. 3g).

4. Additional derivations and data for Fig. 4

4.1. Derivation of linear equation in main text Fig. 4c, for competitive mechanism

A further standard result for competitive inhibitory mechanisms is that^{9,12}

$$K_{d\text{-enzyme-apparent}} = K_{d\text{-enzyme-actual}} (1 + [I] / K_I) \quad (\text{S6})$$

where $K_{d\text{-enzyme-apparent}}$ is the apparent dissociation constant of substrate from the enzyme (factoring in the effect of a competitive inhibitor), $[I]$ is the concentration of the competitive inhibitor, and K_I is the dissociation constant of inhibitor from the enzyme (in the absence of substrate). This additional property of classic competitive inhibition offers constraints beyond those of main text Eq. 1, and furnishes further means to exclude other inhibitory mechanisms^{9,12}. For example, non-competitive mechanisms feature an unchanging $K_{d\text{-enzyme-apparent}}$ independent of $[I]$, whereas uncompetitive mechanisms exhibit a changing $K_{d\text{-enzyme-apparent}}$ with directionally opposite dependence upon $[I]$. Casting Eq. S6 in terms of our particular DCT/channel mechanism yields the second equation within the main text, which we reproduce here as Eq. S7.

$$K_{d\text{-channel-apparent}} = K_{d\text{-channel}} \cdot [\text{ICDI}] \cdot (1 / K_{d\text{-FRET-peptide}}) + K_{d\text{-channel}} \quad (\text{S7})$$

What of the further significance of Eq. S7 for our mechanistic deductions? Already plausible from the sufficiency of main text Eq. 1 is that the holochannel exhibits a competitive inhibitory mechanism. Beyond this, experimental evaluation of Eq. S7 furnishes an extraordinary test of whether ICDI competition with apoCaM for the PreIQ3-IQ segment comprises the actual suite of molecular interactions that underlie holochannel competition. This is because $K_{d\text{-channel-apparent}}$ comes from holochannel measurements, whereas $K_{d\text{-FRET-peptide}}$ comes from FRET 2-hybrid peptide data. If Eq. S7 is not satisfied, then ICDI competition with apoCaM for the PreIQ3-IQ segment is epiphenomenological, and does not actually underlie holochannel competition. Hence, the substantiation of Eq. S7 in main text Fig. 4c furnishes important support that we have correctly identified the actual molecular interactions underlying holochannel competition. This is a significant result given the multiplicity of potential CaM binding segments on voltage-gated channels^{2,13}. Our overall strategy should prove generally useful for dissecting mechanism in macromolecules with several regulatory sites.

A final set of insights comes from the regression analysis of Eq. S7 (shown in main text Fig. 4c). The y -intercept and slope yield molecular parameters that are difficult to deduce by other means. The intercept yields the affinity of the core channel for apoCaM in the absence of inhibitor (~ 10 nM), and the slope can then be used to calculate the local concentration (at the IQ site) of the intramolecular ICDI element (~ 15 μM). These values might be 'effective' parameters if there is local enrichment of apoCaM concentration near channels¹⁴, akin to partition coefficient alteration of permeant ion concentration at the membrane interface of GHK channels¹⁵.

4.2. Excluding even a mixed allosteric-competitive inhibitory scheme via Eq. S7

A highly nuanced allosteric scheme, termed a mixed allosteric-competitive inhibitory mechanism, is the most difficult to exclude^{9,12} (Fig. S4.2a). Here, apoCaM and ICDI elements do not bind to the same channel sites; however, the binding of ICDI renders apoCaM binding to the channel more difficult. In other words, the binding of apoCaM to state 2 is easier than to state 1 ($K_d' > K_d$). Channels lacking apoCaM exhibit no CDI (states 1 and 2); channels bound only to apoCaM and not ICDI exhibit full strength CDI_{max} (state 3); and channel bound to both apoCaM and ICDI (state 4) can also exhibit CDI with strength $f \cdot CDI_{\text{max}}$ ($0 \leq f \leq 1$). Because overexpression of CaM fully recovers CDI to a common CDI_{max} level, f would have to be equal to unity in our considerations. In this case, the mixed scheme will behave entirely according to main text Eq. 1, rendering this nuanced allosteric mechanism most difficult to exclude. Specifically,

$$CDI = CDI_{\max} \cdot \frac{[apoCaM]}{[apoCaM] + K_{d\text{-channel-apparent}}} \quad (S8)$$

just as in the case of the classic competitive inhibitory mechanism (Eqs. S1 and S2). The saving grace comes with consideration of the specific dependence of $K_{d\text{-channel-apparent}}$ upon $[I]$:

$$K_{d\text{-channel-apparent}} = K_{d\text{-channel}} \cdot \frac{(1 + [I]/K_I)}{(1 + [I]/K_X)} = K_{d\text{-channel}} \cdot \frac{(1 + [I]/K_I)}{(1 + [I]/(\alpha \cdot K_I))} \quad (S9)$$

where $K_{d\text{-channel}}$ is the dissociation constant of apoCaM from the channel in the absence of inhibitor (from states 3 to 2 in Fig. S4.2a); K_I is the dissociation constant of ICDI inhibitor from the channel in the absence of apoCaM (from states 1 to 2 in Fig. S4.2a); and K_X is the dissociation constant of ICDI inhibitor from the channel with apoCaM bound (from states 4 to 3 in Fig. S4.2a). For convenience, we

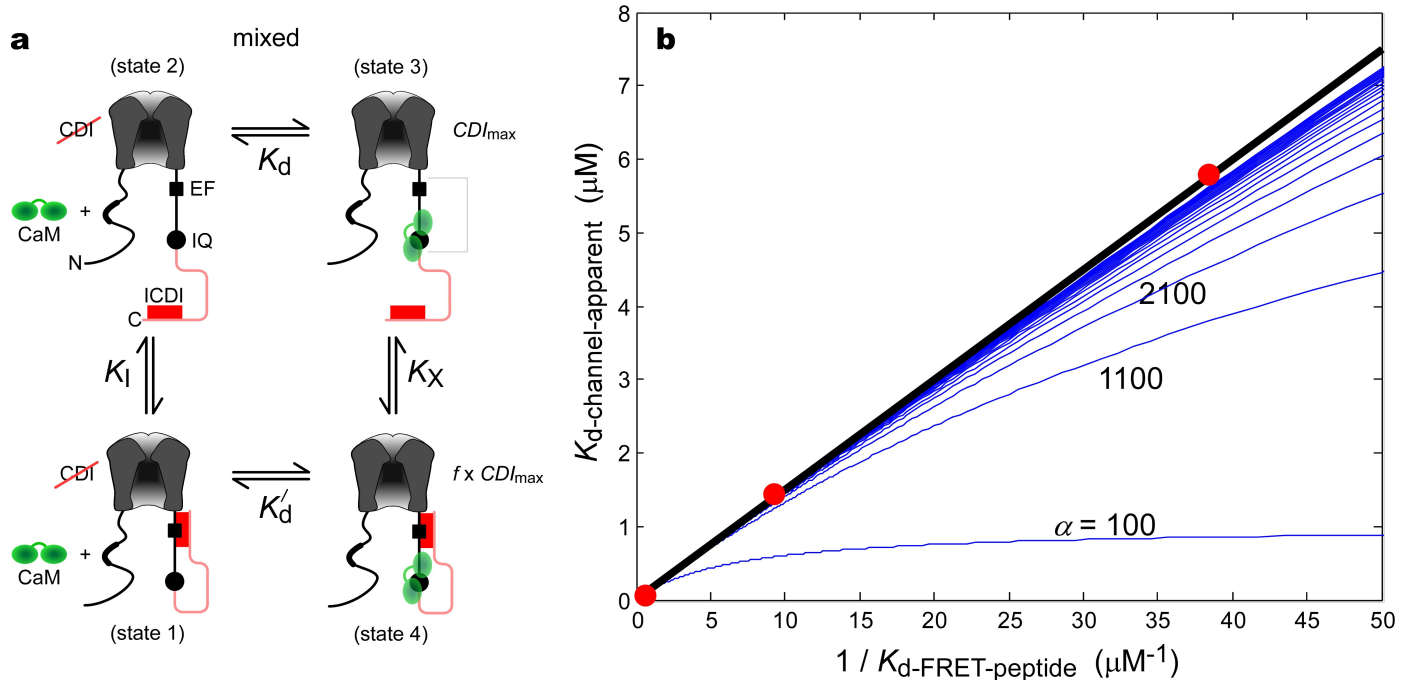


Fig. S4.2 Analysis affiliated with main text Eq. 2 excludes mixed allosteric-competitive mechanism. **a**, Schematic diagram of mixed allosteric-competitive mechanism. **b**, Fit of Eq. S8 to data of main Fig. 4c. α parameter (where $K_X = \alpha \cdot K_I$) must be greater than 1100 to fit data, thereby excluding mixed model, for all practical purposes.

set $K_X = \alpha \cdot K_I$, where $\alpha > 1$ implies that occupancy of state 4 is less likely than state 1. If α is sufficiently larger than 1, then we recover a classic competitive inhibitory mechanism (Eq. S9 becomes Eq. S7). Since $K_I = K_{d\text{-FRET-peptide}}$, we can fit the data in main text Fig. 4c with Eq. S8 to estimate the value of α . We use $K_{d\text{-channel}} \sim 10$ nM and $[I] \sim 15$ μ M, as obtained from linear regression analysis of Eq. S7 to data in main text Fig. 4c, because the y -intercept and initial slope of Eq. S9 would be the same. Fig. S4.2b shows fits of Eq. S9 (blue curves) to data (red symbols and linear fit in black reproduced from main text Fig. 4c). The most saturating blue curve is obtained with $\alpha = 100$, and subsequent curves utilize $\alpha = 1100, 2100, 3100 \dots$ (as labeled). Even a conservative estimate indicates that α is certainly greater than 1100; this large value argues that, for all practical purposes, a classic competitive inhibitory mechanism holds true. This conclusion illustrates a final and powerful use of the analysis affiliated with Eq. S7 (main text Fig. 4c).

4.3. Neuromodulin coexpression experiments in main text Fig. 4e

In main text Fig. 4e (far right), we coexpressed the long variant of human Cav1.3 channels with rat neuromodulin (NP058891), wherein the IQ domain was engineered to avoid PKC variability via for S41A mutation (as in Supplemental 3.1). As a control, we also coexpressed an S41D mutation of rat neuromodulin that altogether eliminates apoCaM binding to neuromodulin. Channel CDI in this

control ($f_{50} = 0.41 \pm 0.04$, $n = 5$) was no different than for channels expressed alone without neuromodulin (main text Fig. 4e, middle), confirming that the neuromodulin effect (main text Fig. 4e, far right) was indeed via buffering of apoCaM.

5. Supplemental information references

1. C. D. DeMaria, T. W. Soong, B. A. Alseikhan et al., *Nature* **411** (6836), 484 (2001).
2. I.E. Dick, M.R. Tadross, H. Liang et al., *Nature* **451**, 830 (2008).
3. M. G. Erickson, H. Liang, M. X. Mori et al., *Neuron* **39** (1), 97 (2003).
4. P. S. Yang, B. A. Alseikhan, H. Hiel et al., *J. Neurosci.* **26** (42), 10677 (2006).
5. H. Liang, C. D. DeMaria, M. G. Erickson et al., *Neuron* **39** (6), 951 (2003).
6. D. J. Black, J. Leonard, and A. Persechini, *Biochemistry* **45**, 6987 (2006).
7. J.T. Hulme, V. Yarov-Yarovoy, T.W. Lin et al., *J. Physiol. (Lond.)* **576**, 87 (2006).
8. A. Singh, M. Gebhart, R. Fritsch et al., *The Journal of biological chemistry* **283** (30), 20733 (2008).
9. C.R. Cantor and P.R. Schimmel, *Biophysical Chemistry: The behavior of biological macromolecules* 11 ed. (Macmillan, 1980).
10. D. Chaudhuri, B. A. Alseikhan, S. Y. Chang et al., *J. Neurosci.* **25** (36), 8282 (2005).
11. M. G. Erickson, B. A. Alseikhan, B. Z. Peterson et al., *Neuron* **31** (6), 973 (2001).
12. A.L. Lehninger, D.L. Nelson, and M.M. Cox, *Principles of biochemistry*, 4 ed. (Macmillan, 2005).
13. K. Dunlap, *J. Gen. Physiol.* **129** (5), 379 (2007); J. Kim, S. Ghosh, D. A. Nunziato et al., *Neuron* **41** (5), 745 (2004); G. S. Pitt, R. D. Zuhlke, A. Hudmon et al., *The Journal of biological chemistry* **276** (33), 30794 (2001); L. Xiong, Q. K. Kleerekoper, R. He et al., *The Journal of biological chemistry* **280** (8), 7070 (2005).
14. M. X. Mori, M. G. Erickson, and D. T. Yue, *Science* **304** (5669), 432 (2004).
15. B. Hille, *Ionic channels of excitable membranes*. (Sinauer Associates, Sunderland, MA, 1984).